Available online at www.sciencedirect.com

ScienceDirect

Advances in Space Research 63 (2019) 1404–1424

ADVANCES IN SPACE RESEARCH (a COSPAR publication)

www.elsevier.com/locate/asr

Solar physics with the Square Kilometre Array

A. Nindos [a,*], E.P. Kontar [b], D. Oberoi [c]

[a] Physics Department, University of Ioannina, GR-45110 Ioannina, Greece
[b] School of Physics & Astronomy, University of Glasgow, G12 8QQ Glasgow, UK
[c] National Centre for Radio Astrophysics, Tata Institute of Fundamental Research, Pune 411007, India

Received 30 April 2018; received in revised form 16 October 2018; accepted 17 October 2018
Available online 24 October 2018

Abstract

The Square Kilometre Array (SKA) will be the largest radio telescope ever built, aiming to provide collecting area larger than 1 km^2. The SKA will have two independent instruments, SKA-LOW comprising of dipoles organized as aperture arrays in Australia and SKA-MID comprising of dishes in South Africa. Currently the phase-1 of SKA, referred to as SKA1, is in its late design stage and construction is expected to start in 2020. Both SKA1-LOW (frequency range of 50–350 MHz) and SKA1-MID Bands 1, 2, and 5 (frequency ranges of 350–1050, 950–1760, and 4600–15,300 MHz, respectively) are important for solar observations. In this paper we present SKA's unique capabilities in terms of spatial, spectral, and temporal resolution, as well as sensitivity and show that they have the potential to provide major new insights in solar physics topics of capital importance including (i) the structure and evolution of the solar corona, (ii) coronal heating, (iii) solar flare dynamics including particle acceleration and transport, (iv) the dynamics and structure of coronal mass ejections, and (v) the solar aspects of space weather. Observations of the Sun jointly with the new generation of ground-based and space-borne instruments promise unprecedented discoveries.

Keywords: Sun; Sun:radio radiation; Sun:corona; Sun:flares; Sun:coronal mass ejections

1. Introduction

Although solar physics is one of the most mature branches of astrophysics, the Sun confronts us with a large number of outstanding problems that are fundamental in nature. These problems include the determination of the structure and dynamics of the solar atmosphere, the magnetic field evolution in the chromosphere and corona, coronal heating, the physics of impulsive energy release, energetic particle acceleration and transport, the physics of coronal mass ejections (CMEs) and shocks, as well as the solar origin of space weather drivers.

Solar radio astronomy has already provided important insights into these problems because (i) two of the natural frequencies of the solar magnetized plasma, the electron plasma frequency, ν_{pe}, and the electron gyrofrequency, ν_{ce}, fall into the radio band, and (ii) radio emission is sensitive not only to the properties of radiating electrons but also to the properties of the ambient plasma and magnetic field. However, the full exploitation of the diagnostic potential of solar radio emission is instrumentally demanding because solar radio sources can be both small ($\lesssim 1''$ in localized episodes of energy release; e.g. see the VLBI observations by Tapping et al., 1983) and large ($\gtrsim 1°$ in radio CMEs; e.g. Bastian et al., 2001), weak (< 1 sfu in the quiet Sun) and strong ($>10^5$ sfu in large flares). Furthermore flux variations down to msec time scales and narrow-band features of relative bandwidth down to 1–0.01% are often observed in coherent flare/CME-related bursts. Therefore,

* Corresponding author.
E-mail addresses: anindos@uoi.gr (A. Nindos), Eduard.Kontar@glasgow.ac.uk (E.P. Kontar), div@ncra.tifr.res.in (D. Oberoi).

https://doi.org/10.1016/j.asr.2018.10.023
0273-1177/

non-incremental progress in solar radio astronomy requires high-cadence, high-sensitivity, large dynamic range, snapshot imaging interferometric observations over a large bandwidth with adequate $u-v$ coverage and angular and frequency resolution. Unfortunately, there has been no radio instrument that is capable of meeting all of the above requirements.

Historically, solar radio observations have been performed along two lines: spectroscopy and imaging observations. Spectroscopic observations (primarily at decimeter, meter, and decameter wavelengths) provide spatially unresolved data with time and frequency resolution of about $\lesssim 1$ s and $\lesssim 1$ MHz, respectively, while interferometric imaging observations take place at discrete frequencies providing data with angular resolution from a few arcsec to a few arcmin depending on the frequency of observations.

During the last couple of decades, old solar-dedicated and general-purpose radio interferometers have been upgraded and some of them are now capable of performing solar radio spectroscopic imaging and the same is/will be true for new instruments (either already deployed or under construction). The solar-dedicated instruments include the upgraded Expanded Owens Valley Solar Array (EOVSA; see Gary et al., 2012), the Mingantu Ultrawide Spectral Radioheliograph (MUSER; see Yan et al., 2016), the Nançay Radioheliograph (NRH; see Kerdraon and Delouis, 1997), the Nobeyama Radioheliograph (NoRH; see Nakajima et al., 1994), and the upgraded Siberian Radioheliograph (Siberian RH; see Lesovoi et al., 2014) while the general-purpose instruments include the expanded Karl G. Jansky Very Large Array (VLA; see Perley et al., 2011), the Low Frequency Array (LOFAR, e.g. van Haarlem et al., 2013), the Murchison Widefield Array (MWA, see Tingay et al., 2013; Bowman et al., 2013), the Long Wavelength Array (LWA; see Ellingson et al., 2009), and the Giant Metre-wave Radio Telescope (GMRT; see Swarup et al., 1991). A summary of the specifications of these instruments (in alphabetical order) is given in Table 1.

The Square Kilometre Array (SKA) will be a general-purpose radio instrument whose construction is expected to start in 2020 and whose characteristics will significantly exceed the capabilities of the instruments of Table 1. It will be capable of performing solar observations which will have the potential to transform solar radio astronomy in particular, and solar physics in general. A testament to this argument is the important results that have come out of data obtained with SKA's "precusor" and "pathfinder" projects: the LOFAR (e.g. Morosan et al., 2014, 2015, 2017; Reid and Kontar, 2017; Kontar et al., 2017b; Chen et al., 2018), the MWA (e.g. Oberoi et al., 2011; Mohan and Oberoi, 2017; McCauley et al., 2017; Suresh et al., 2017; Cairns et al., 2018; Sharma et al., 2018), the VLA (Spangler and Whiting, 2009; Chen et al., 2013; Kooi et al., 2014; Chen et al., 2015), and the LWA (Tun Beltran et al., 2015).

This paper is organized as follows. In Section 2, we outline the major features of the SKA and in Section 3 we discuss the particulars of solar observations with it. In Section 4 we briefly outline solar radio emission mechanisms, and in Sections 5–9 we discuss open issues on solar radio astronomy and how the relevant SKA observations can bring results of transformative nature. In Section 10 we outline possible synergies between the SKA and other instruments, and in Section 11 we summarize the paper. Note that in this paper we restrict ourselves only to the discussion of solar physics problems that could be addressed by SKA observations; a discussion of heliospheric physics problems which will be addressed by the SKA lies outside the scope of this paper. A broader but shorter review discussing SKA's potential impact on both solar and heliospheric physics is available in Nakariakov et al. (2015).

2. Overview of the instrument

2.1. Basic features

This section is based on information from various documents that can be found at https://astronomers.skatelescope.org. The SKA is an international project to build the world's largest and most sensitive radio telescope. When completed the collecting area of the instrument will be about one square kilometer, hence its name. The instrument will be built in two phases, known as SKA1 and

Table 1
Instruments capable of performing solar radio spectroscopic imaging.

Instrument	Frequency range (GHz)	Spectral resolution (MHz)	Time resolution (ms)	Angular resolution (″)	Solar dedicated
EOVSA	1–18	50	20	3–57	Yes
GMRT	0.15–1.50	0.05	100	2–20	No
LOFAR	0.03–0.24	0.1	10	60–540	No
LWA	0.02–0.08	0.008	1	2–8[a]	No
MUSER	0.4–15	25	25–200	1.3–50	Yes
NoRH	17, 34	1700	100	6–12	Yes
NRH	0.15–0.45	23–48	250	18–240	Yes
MWA	0.08–0.30	0.04	500	16–60	No
Siberian RH	4–8	10	560	15–30	Yes
VLA	1–50	1	100	1–35	No

[a] Currently only two LWA stations have been deployed; the angular resolution cited here refers to the originally envisaged array.

SKA2. SKA1 will correspond to about 10% of the final collecting area and its deployment will start in 2020 while commissioning activities are expected to start in 2024. SKA2 will correspond to the full final system and its construction will start, subject to the performance of SKA1, after 2030.

The SKA1 will consist of two arrays, SKA1-LOW and SKA1-MID, that will be built in Australia and South Africa, respectively. The expected configuration of the two arrays is presented in the geophysical maps of Fig. 1. The maximum baselines of the arrays is expected to be about 65 km for SKA1-LOW and about 150 km for SKA1-MID.

The SKA1-LOW will observe from ~50 to 350 MHz and it will be deployed in the Murchison desert of Western Australia (central coordinate 26°41′49″S 116°37′53″E) in the same region as the Australian SKA Pathfinder (ASKAP) and MWA arrays. It will include about 131,000 simple antennas (e.g. log-periodic dual-polarization dipole elements) that are arranged in 100-m-diameter stations each hosting 90 elements. In each station the signal of all elements will be added together electronically, in phase, allowing the formation of an "aperture array" (see Fig. 2, left). The separation between stations will increase from the central part of the array toward its outer edge, reaching several kilometers there.

The SKA1-MID will observe in the range from 350 MHz to 15.3 GHz which will be divided into three frequency bands (Band 1: 0.35–1.05 GHz, Band 2: 0.95–1.76 GHz, and Band 5: 4.60–15.30 GHz). The array will include 133 15-m-diameter dishes (see Fig. 2, right) and will also incorporate the 64 13.5-m-diameter dishes of the MeerKAT array. SKA1-MID will be deployed in the Karoo desert of South Africa, 500 km north of Cape Town (central coordinate 30°43′16″S 21°24′40″E). The dishes will be placed along a three-armed spiral (see Fig. 1, left); along each arm the separation of dishes will increase with the distance from the center of the array.

In Table 2 we present a summary of SKA1's specifications. They represent an unprecedented improvement over all existing radio telescopes and will allow SKA1 to contribute to decisive advances in practically all branches of modern astrophysics (e.g. see Braun et al., 2015, and references therein).

The SKA2 detailed specifications will be finalized depending on the progress of SKA1. It is anticipated that both the SKA2-LOW and -MID arrays will form five 300-km-long spirals. There are plans for the deployment of a few extra dishes to southern and central African states (i.e. away from the instrument's core spiral configuration) that will yield maximum baseline of about 3000 km.

The development of an instrument of such size poses difficult construction and engineering problems. Furthermore, even the SKA1 will produce data rates of several TB/s whose processing will require central supercomputers capable of in excess of 100 petaflops (i.e. 10^{17} floating point operations per second) of raw processing power. The technical consortia that are responsible to build the SKA rely on the recent huge progress both in the design of antennas and wide-bandwidth feeds and in the transport and process of large amounts of data. These recent developments have resulted in the development of instruments (either new or upgraded old ones) that are engaged in SKA-related technology and science studies. These instruments are called "SKA precursors" (if located at future SKA sites, e.g. the MWA) or "SKA pathfinders", the latter include the VLA, the LOFAR, the GMRT and others (for a complete census, see https://tinyurl.com/yaageuhz).

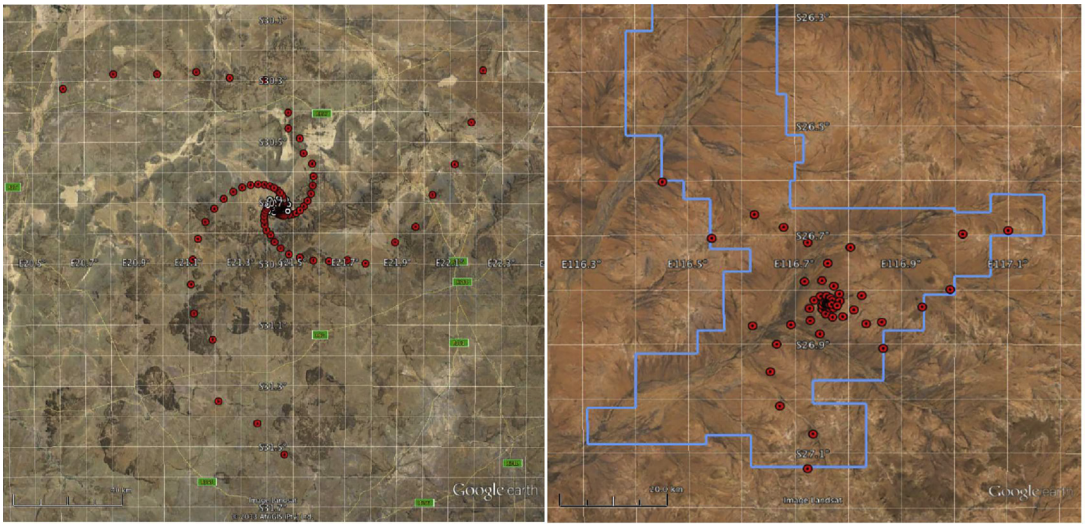

Fig. 1. Geophysical maps with the SKA1-MID (left) and SKA1-LOW (right) configurations. The horizontal lines at the bottom left corners of the maps correspond to 40/20 km (left/right map). Image credit: SKAO.

Fig. 2. Artist's impression of the SKA1-LOW aperture arrays (left) and SKA1-MID dishes (right). Image credit: SKAO.

Table 2
Summary of SKA1 specifications.

Parameter	SKA1-LOW value	SKA1-MID value
Frequency range (MHz)	50–350	350–15,300
Angular resolution (″)	4–24	0.025–1
Time resolution (s)	0.001–9	0.001–9
Frequency resolution (kHz)	5	15–76
Field of view (deg^2)	2–39	$\leqslant$1.4
Largest angular structure (′)	60–500	15–80
Sensitivity ($\times 10^{-3}$ sfu)	0.46–4.00	0.16–0.90

2.2. Modes of observations and data analysis

SKA is an evolving project and several of its engineering, hardware and software aspects have not been finalized yet. The technical aspects of the SKA project (including software) are outlined in Hall (2005) while more up-to-date information can be found at https://astronomers.skatelescope.org.

The signals collected from MID and LOW arrays will be digitized and fed into the instument's "Central Signal Processor" (CSP).[1] CSP's main task will be the collection, correlation, filtering, and analysis of the observational data, according to the requirements of each observing run. To meet the requirements imposed by the SKA's specifications, the CSP will utilize extremely fast computers (see Section 2.1). Furthermore, to reduce power consumption, most of the signal processing will be done in Field-Programmable Gate Arrays (FPGAs) and Graphics Processing Units (GPUs).

Telescope resources will be enhanced by allowing users of both telescopes (MID and LOW) to divide collecting area into up to 16 subarrays and operate each subarray as an independent instrument. Users will be allowed to schedule their observing run, select observing mode, and determine the timeline of their observations for each subarray independently.

The SKA will conduct primarily two kinds of observations, interferometric imaging and beamforming. All interferometric imaging observations will, by definition, be spectroscopic. For a given subarray operating in "interferometric mode", each pair of antennas will be cross-correlated to provide full-polarization visibilities across the requested bandwidth and number of channels.

In the "beamforming mode" each subarray can form several tied-array beams and process data for each beam independently:

- SKA1-MID will be able to form up to 1500 "Pulsar Search" beams, spread over up to 16 subarrays, each covering 300 MHz, based on the selected antennas within 10 km of the subarray center. Similar operations are anticipated for SKA1-LOW for up to 500 beams.
- Both MID and LOW telescopes will be able to form up to 16 "Pulsar Timing" beams. The setup will be similar to the "Pulsar Search" one, with the exception that each beam will cover full input bandwidth for the observing band.

The output of the CSP will be forwarded to the "Science Data Processor" (SDP)[2] for further reduction and post-processing in order to derive scientifically useful results. The objective of the SDP subsystem is to build the necessary data analysis software and pipelines, and the necessary hardware platform on which these "realtime" or pseudo-realtime pipelines will run. The details of the SDP data products are still being worked out but it is anticipated that at least calibrated visibilities and continuum and/or spectral-line image cubes will be made available to SKA scientists. The SDP operations will naturally take place

[1] For more details see https://www.skatelescope.org/csp.

[2] For more details see https://www.skatelescope.org/sdp.

close to the telescope sites and the results will be stored somewhere not too far away. There is a plan/desire to have SKA data centers set up across the world, which will host copies (or subsets) of the SKA data archives, where scientists can access the processed SKA data products. These centers are expected to be places where the vast majority of the scientists will interact with and analyze the SKA data. Formally, they lie outside the scope of the SKA project and are being financed independently by the SKA member countries.

SKA is expected to have a set of Key Science Projects (KSPs) (typically with observing requirements of order 1000 h or more) and also "Principal Investigator" (PI)-driven projects. The KSPs are still being formulated and the division of observing time between KSPs and PI-driven projects is unclear. SKA will also have the requirement to distribute observing time roughly in proportion to the contributions by the member countries, although final decisions have not been reached yet.

3. Solar observations with the SKA1

Scientists interested in using the SKA for their research have formed "Science Working Groups" (SWGs) which are advisory groups that provide input to the SKA Organization (SKAO) "... on the design, commissioning, and future operations of the SKA that are likely to affect the Observatory's scientific capability, productivity, and user relations".[3]

One of them is the "Solar, Heliospheric and Ionospheric" (SHI) SWG.[4] It has more than 60 members from four continents and 20 countries and it is currently chaired by E.P. Kontar (Glasgow) and D. Oberoi (Pune). The scientific interests of the SHI SWG include the quiet Sun, non-flaring active regions (ARs), solar flares, CMEs, the solar wind, the Sun-Earth system, and the ionosphere.

The SHI group investigates the feasibility, hardware-wise, of solar observations with both SKA1-LOW and -MID. The SKA will be able to observe the Sun both in interferometric imaging and beamforming modes (see Section 2.2).

Low-frequency solar radio burst observations are in many ways similar to observations of bright astrophysical radio sources and many general purpose techniques can be ported to solar observations. As for the SKA1-MID, it has been established that: (1) the dishes can be pointed to the Sun without raising the temperature of the receiver box by an unacceptable amount, and (2) the low-noise amplifiers themselves are not expected to be saturated by the slowly-varying solar radio emission or even solar radio bursts because they have been designed to have sufficient head-room to be able to deal with the occasional presence of strong radio-frequency interference. On the other hand, for the digital sampling of the data there will be a need to adjust the gains/attenuations at appropriate stages in the signal chain to ensure that the sampling levels chosen are appropriate for the range of the voltages spanned by the solar signal.

Another important issue is that simultaneous observations with the LOW and MID arrays (especially of transient phenomena) will be very difficult due to the large separation of the two arrays. Simultaneous observations at the three SKA1-MID Bands (see Section 2) will be possible, in principle. This will, however, require configuring the array as three independent sub-arrays operating at each of the three bands.

Beamforming observations of the Sun will be possible by using the pulsar setup briefly described in Section 2.2. The observing requirements of the pulsar setup in terms of time and frequency resolution will be more extreme than those needed for solar observing. The large number of beams that will be provided simultaneously will be sufficient to tile the SKA1-MID beam and the whole Sun in the case of SKA1-LOW.

As mentioned in Section 2.2, the development of the SDP is still in its early phases. Details of the data products it will eventually deliver are under discussion and the computational requirements to meet them are being estimated. No software tailored to the unique snapshot spectroscopic imaging requirements of solar observations has yet been developed either by the SKA project or by the SHI SWG. However, the solar and heliospheric science team of the MWA, a SKA precursor, has recently developed an automated interferometric solar imaging pipeline, a first step towards building experience and understanding the issues associated with solar imaging from this class of instruments (Mondal et al., 2018).

4. Solar radio emission mechanisms

The electrons that produce solar radio emission can be either thermal or nonthermal and the emission mechanisms either coherent or incoherent (see Dulk, 1985; Nindos et al., 2008; Pick and Vilmer, 2008, for more detailed reviews).

The most usual incoherent mechanisms are free-free emission and gyroemission. The former is generated when free electrons interact with ambient ions via Coulomb forces and is therefore ubiquitous. Radio emission is produced when the relevant particle populations are part of the same thermal distribution and provides diagnostics of temperature, density, and (to some extent) magnetic field.

Gyroemission is produced when free electrons are accelerated in a magnetic field because they experience the magnetic part of the Lorentz force. In the literature gyroemission is referred to as gyroresonance emission when nonrelativistic electrons are involved and gyrosynchrotron when mildly relativistic electrons are involved. In the former case, the emission comes from hot ($T_e \sim 10^6$ K)

[3] Excerpt taken from the Terms of Reference for SKA's SWGs (see https://tinyurl.com/ycmtjdrt).

[4] https://www.skatelescope.org/shi/.

thermal plasma interacting with magnetic fields in excess of 100 G. It is very sensitive to magnetic field strength and orientation (e.g. Zheleznyakov, 1970) and generates microwave emission at low harmonics of the gyrofrequency above sunspots with strong magnetic field. Gyrosynchrotron is the basic microwave process in flares and is produced by thermal or nonthermal energetic electrons (tens of keV to several MeV) at harmonics 10–100 of the gyrofrequency. In addition to the magnetic field strength and orientation, the emission is also sensitive to the properties of the radiating electrons (e.g. Fleishman and Melnikov, 2003a,b).

The most important coherent emission mechanism is the plasma emission mechanism (e.g. Melrose, 1980). It involves the formation of non-equilibrium electron distributions, which excite plasma waves via nonlinear processes. The plasma waves can be converted in part to electromagnetic waves at the plasma frequency ($\nu_{pe} = 9\sqrt{n_e}$ kHz, where n_e is the number density in cm^{-3}) and/or its second harmonic, $2\nu_{pe}$, via scattering off thermal ions or coupling to ion-acoustic waves. Radio emissions via the plasma mechanism are called type III bursts when they are associated with upward-propagating beams of energetic electrons and type II bursts when the energetic electrons are accelerated in MHD shocks.

Transient plasma emission is often the brightest solar emission and is typically observed at decimeter and longer wavelengths. The relevant flux densities may exceed 10^5 sfu (e.g. Pick et al., 2005b) while the associated brightness temperatures may lie in the range of 10^9–10^{12} K (Saint-Hilaire et al., 2013). On the other hand the large-scale quiet free-free flux density may range from less than 1 sfu to more than 100 sfu (T_b from $\leqslant 10^6$ to $\sim 10^4$ K, respectively) as we move from low to high frequencies in the SKA frequency range (e.g. Benz, 2009). Furthermore, gyroresonance-associated flux densities may reach 10 sfu ($T_b \sim 10^6$ K) while the gyrosynchtron mechanism may yield flux densities in excess of 1000 sfu ($T_b > 10^7$ K) at short microwaves (e.g. Nita et al., 2002), and as weak as 0.01 sfu ($T_b \sim 100$ K) in the meter-wave band (e.g. Bastian et al., 2001; Tun and Vourlidas, 2013).

The above discussion indicates that high dynamic range imaging is needed to map both the features associated with plasma emission and those associated with other mechanisms. Probably the most extreme requirements are posed by the need to map both the plasma and free-free emissions in CMEs (see Section 9.1) where a dynamic range of at least 10^4 is needed. The dynamic range of SKA1 images will certainly exceed that value because one of its precursors (i.e. the MWA) is already able to exceed it (Mondal et al., 2018, submitted for publication). SKA1 images with dynamic range of about 10^5 appear to be feasible although one cannot guarantee values of about 10^6 or higher.

The weakest solar radio emissions are associated with tiny transient activity originated from either free-free or gyrosynchrotron mechanism (see Section 7). In the literature the weakest among such events have been presented by Krucker et al. (1997) (flux densities down to 0.002 sfu in events detected at 15 GHz). It is not known whether there exists a lower limit for the flux density of such weak events but SKA1 unprecedented sensitivities (see Table 2) will help us detect them down to levels not achievable before.

5. Plasma diagnostics of the nonflaring Sun

In the weak magnetic field regions of the non-flaring Sun, the radio emission comes from the free-free mechanism. The radiation is formed in local thermodynamic equilibrium (LTE) and the source function is Planckian. For radio frequencies the Rayleigh-Jeans approximation is valid and the observed intensity is proportional to the kinetic temperature of the emitting plasma for optically thick sources (in stark contrast to the situation in optical and UV wavelengths).

The highest frequencies that will be accessible with SKA1 ($3 \lesssim \nu < 15$ GHz) are optically thin (an example appears in the 17 GHz image of Fig. 3) and we see down below the transition region (TR): the higher the frequency the deeper we see. At such high frequencies the only regions above the chromosphere that may become optically thick are associated with sunspots of strong magnetic field where gyroresonance absorption could become significant. At frequencies between 1 and 3 GHz the non-flaring corona is optically thin except over active regions where hot, dense loops may render it optically thick to free-free (e.g. White, 1999). At decimeter and longer wavelengths the emission is optically thick and TR/coronal brightness temperatures are expected. Examples of images, produced using rotational synthesis imaging, at such low frequencies (obtained with the NRH at 150–432 MHz) appear in Fig. 3. The figure shows that the similarity of the soft X-ray image with the NRH images decreases as frequency decreases. This cannot be attributed to a spatial resolution effect only (Kontar et al., 2017b). Apart from refraction effects that are at work in radio (e.g. Alissandrakis, 1994; Shibasaki et al., 2011), the optical depth of the radio emission is appreciable. Therefore these radio images probe higher layers of the corona, and lower-lying X-ray-emitting structures are obscured by overlying dense material. The same arguments explain the little resemblance between the NRH images and the 17 GHz image.

Using the SKA1 frequency bands we will be able to sample, with unprecedented angular and spectral resolution, the thermal state of optically thick structures (e.g. the quiet Sun, coronal holes, active regions, and filaments) at heights above the chromosphere. We also note that there is a lack of imaging of the Sun at frequencies from 0.45 GHz to 1 GHz. With SKA1-MID Bands 1 and 2 (frequencies from 0.35 to 1.76 GHz) we will be able to image that frequency range (MUSER, however, may obtain images at that frequency range before SKA1).

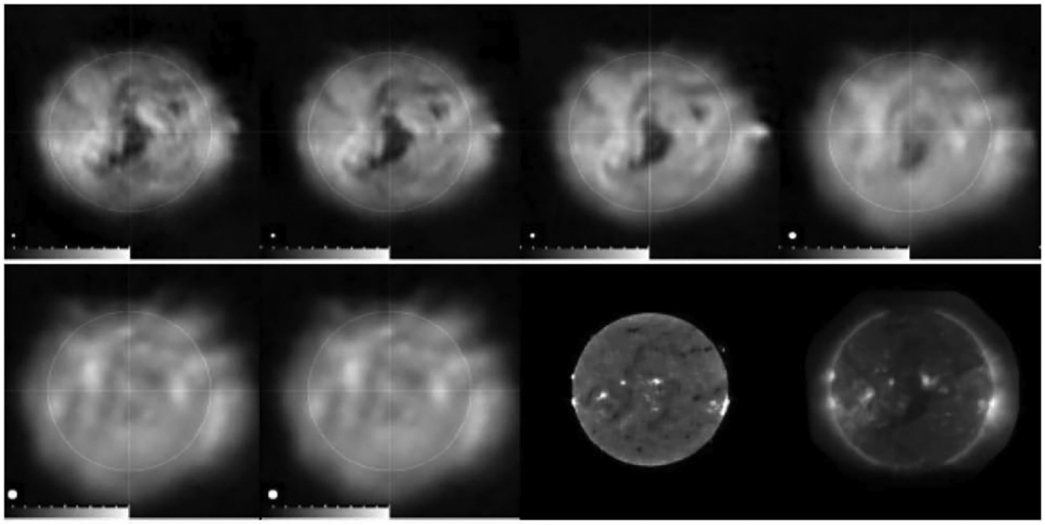

Fig. 3. Images of the Sun on 2004 June 27. From left to right and from top to bottom: NRH images at 432, 410, 327, 236, 164, and 150 MHz, NoRH image at 17 GHz and soft X-rays image from SXI on board GOES12. After Mercier and Chambe (2009). Reproduced by permission of the AAS.

6. Coronal magnetography

Due to inherent difficulties in measuring the Zeeman effect in the corona (Lin et al., 2004), radio methods are of primary importance in obtaining quantitative information about its magnetic field.

6.1. Coronal magnetic field from gyroresonance emission

Gyroresonance emission is a valuable tool for magnetic field measurements above sunspots. There are several publications on the subject particularly after the first modeling of high-resolution observations by Alissandrakis et al. (1980). More recent publications have been reviewed by White and Kundu (1997) and Lee (2007).

The gyroresonance emission observed at a given frequency originates from a narrow iso-gauss layer where the frequency matches a low harmonic of the gyrofrequency (see Fig. 4). The gyroresonance opacity (Zheleznyakov, 1962) is much higher in the *x*-mode than in the *o*-mode, and at the second harmonic than at the third. Above sunspots, the third harmonic is opaque in the *x*-mode but not in the *o*-mode, and the second harmonic is opaque in both modes. Emission from the fundamental is not observed, both because it is obscured by the overlying second harmonic layer and because of propagation effects, while emission at the fourth harmonic can appear at long centimeter wavelengths.

For low photospheric magnetic fields or/and high frequencies both the third and second harmonic layers are below the TR and no strong gyroresonance emission is expected. The third harmonic layer enters into the TR for appropriately higher values of the field or lower frequencies and yields strong, almost 100% polarized, emission (e.g. Shibasaki et al., 1994; Nindos et al., 2000a). The second harmonic layer enters the TR for even higher field intensities or lower frequencies and then the polarization drops. Therefore the brightness temperature spectra of both total intensity (I) and circular polarization (V) show a rapid rise at the wavelength where the third harmonic enters into the TR; the magnetic field at the base of the TR can be estimated from the extrapolation of the V to zero and the equation $\nu = s\nu_{ce}$ with harmonic number $s = 3$. The potential of this technique has been demonstrated in several publications that use OVSA (e.g. Gary and Hurford, 1987, 1994) and RATAN-600 spectral data (e.g. Akhmedov et al., 1986; Korzhavin et al., 2010). Note also that such measurements are now routinely available from RATAN-600 data and can be found at http://www.sao.ru/hq/sun.

SKA1-MID Band 5 (4–15 GHz) observations will provide a brightness temperature spectrum along each line of sight through the gyroresonance source, thereby enabling the assembly of a map of the magnetic field at the base of the TR. Given the fact that when a harmonic layer is opaque the observed brightness temperature is equal to the local electron temperature, the 3D structure of the coronal magnetic field could also be constrained (e.g. Tun et al., 2011) because the SKA1-MID's spectroscopic imaging observations could yield the variation of the magnetic field strength as a function of temperature along each line of sight through the gyroresonance source, provided that one identifies the harmonic(s) that contribute to the gyroresonance emission at each frequency. The dense spectral coverage that will be provided by SKA1 will yield complete sampling of a large part of the TR/coronal volume over sunspots, and therefore continuous magnetic field strength coverage.

6.2. Coronal magnetic field from propagation effects

When radio emission passes through a region where the longitudinal component of the magnetic field changes sign,

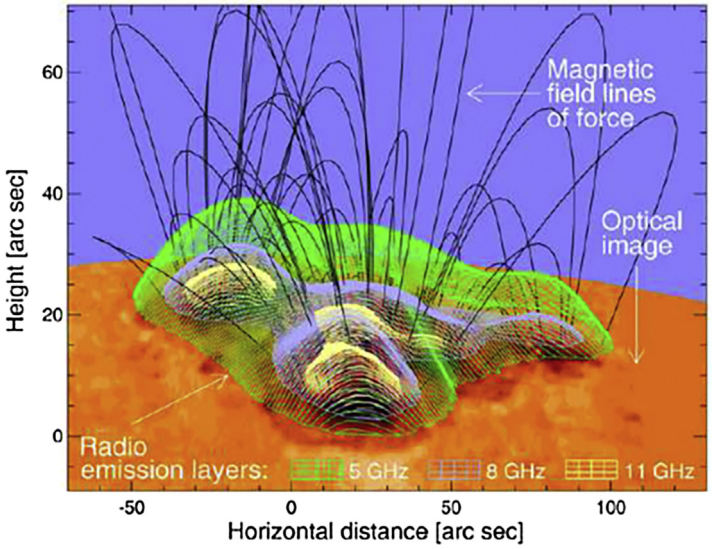

Fig. 4. Iso-Gauss surfaces corresponding to the third harmonic of the gyrofrequency at 5, 8 and 11 GHz, together with lines of force of the extrapolated magnetic field for an active region. From Lee (2007). Reproduced with permission ©Springer Nature.

its sense of circular polarization reverses when the coupling (which depends on the magnetic field strength and the gradient of the angle between the line of sight and the field along the ray path, as well as the electron density and the frequency of observation) between the x- and o-modes is weak and does not change when the coupling is strong (e.g. Bandiera, 1982). For intermediate "critical" coupling the polarization becomes linear. The line that delineates the reversal in the sense of circular polarization ($V = 0$) is known as "depolarization strip".

In depolarization strips one can estimate the magnetic field under some assumption about the electron density (e.g. Kundu and Alissandrakis, 1984). The extension of this method for cases of partial depolarization allows for the computation of a coronal magnetogram over the quasi-transverse layer (i.e. the region where the magnetic field is almost perpendicular to the direction of propagation of the radiation), provided that the intrinsic polarization of the waves is known, for example by using polarization data before the mode coupling occurs (see Ryabov et al., 1999, 2005, for details).

Polarization inversion provides diagnostics about the coronal magnetic field at heights of about 0.05–0.4$R_\odot$, and is independent of the emission mechanism. Therefore all SKA1-MID Bands could be used to exploit the potential of the method: their dense spectral coverage will allow to locate the coronal regions where the field is perpendicular to the line of sight and to derive information about the magnetic field well above the formation height of the microwave emission.

6.3. Magnetic field from free-free emission

The weak polarization of the free-free emission in the sense of the x-mode can be used to determine the longitudinal component, B_l, of the magnetic field: for an optically thin slab above a uniform background it is easy to show that B_l is proportional to the degree of circular polarization, ρ, and the frequency. Things are more complicated in the general case, where physical conditions vary with height. When spectral observations are available, one can use the approximate expression (Bogod and Gelfreikh, 1980; Grebinskij et al., 2000) to determine B_l:

$$B_l \approx 107 \frac{\rho(\%)}{n\lambda}, \tag{1}$$

where B_l is in G, λ is the wavelength in cm, and $n = -\ln T_b / \ln \nu$ the spectral index. This expression allows for temperature variations in the radiation-formation region and its validity is not limited to the optically thin case, although it implicitly assumes constant magnetic field. The combination of SKA1-MID's unprecedented sensitivity and high frequency resolution will allow, for the first time, to constrain the longitudinal component of the coronal magnetic field to a few Gauss.

An extension of the above method could be used to provide estimates of the magnetic field strength of undisturbed streamers at higher altitudes (heliocentric distances of 1.5$R_\odot$ to 2.5$R_\odot$) by measuring the degree of circular polarization of the associated free-free emission using SKA1-LOW observations (see Sastry, 2009; Ramesh et al., 2010b, for details).

7. Coronal heating

Coronal heating remains one of the major unsolved problem in solar physics. The proposed mechanisms to heat the corona (e.g. see Klimchuk, 2006; De Moortel and Browning, 2015, for reviews) are divided into two broad classes: waves and small-scale reconnection events, also known as nanoflares. Acoustic wave heating has been

a favorite for the non-magnetic chromosphere, but it appears that the appropriate waves do not carry enough energy (Fossum and Carlsson, 2005). Other types of waves, such as Alfven waves in the presence of turbulence (van Ballegooijen et al., 2011) could be an alternative.

There have been several efforts to search radio data for small-scale transient events that could potentially contribute to coronal heating. These efforts are partially inspired by the sensitivity of the radio domain to small populations of nonthermal electrons that could arise in the course of reconnection. At microwaves such studies (e.g. White et al., 1995; Krucker et al., 1997; Gary et al., 1997; Nindos et al., 1999; Benz and Krucker, 1999) have shown that tiny transient activity may occur both within and away from ARs and that in several cases the events show flare-like properties being either thermal or nonthermal. At lower frequencies short duration small isolated bursts have also been reported (e.g. Kundu et al., 1986; Ramesh et al., 2010a; Saint-Hilaire et al., 2013; Suresh et al., 2017, see Fig. 5).

Several authors (e.g. Lin et al., 1984; Gary, 1999; Aschwanden et al., 2000; Aschwanden and Parnell, 2002) have computed histograms of the energy distribution in impulsive events using X-ray and EUV data. However, the low energy part of flaring events is poorly known, hence nanoflare heating model (Parker, 1988) evades observational confirmation.

SKA1 could provide significant insights into the coronal heating problem because: (1) it will provide detailed time series of the temperature, density, and magnetic field in various coronal structures (see Sections 5 and 6) from which the rate of energy storage into the corona could be estimated as a function of position and time and then checked against wave heating model predictions, (2) due to its unprecedented sensitivity, angular, temporal and spectral resolution, as well as wide field of view, SKA1 will be able to detect weak, small, short-lived, narrow-band transient events down to levels not achievable earlier, over large parts of the solar disk. The computation of the occurrence rate and energy budget of these events will help us derive more accurate constraints than ever before and evaluate their role in coronal heating.

8. The physics of flares

Through magnetic reconnection, flares release large amounts of magnetic energy stored in the corona which accelerates particles and heats extended layers of the solar atmosphere. Accelerated particles emit at radio wavelengths, X-rays, and in some cases gamma-rays (see Holman et al., 2011, for a review). The hard X-rays typically arise from the interaction of electrons with energies from a few tens of keV to a few hundreds of keV with chromospheric plasma via the nonthermal free-free mechanism. On the other hand, radio emission may arise either from suprathermal electrons that produce coherent radio emission due to plasma instabilities or from mildly relativistic electrons that emit nonthermal gyrosynchrotron radiation. X-ray and radio observations complement each other (e.g. White et al., 2011) and both are essential to study particle acceleration and transport. Radio observations provide the advantage that not only are they sensitive to anisotropies in the electron distribution function, but also uniquely sensitive to the magnetic field.

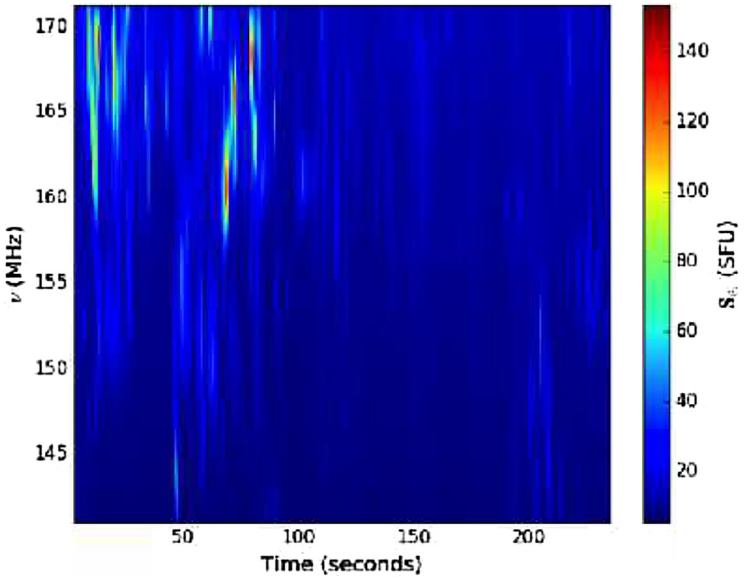

Fig. 5. MWA dynamic spectrum with numerous nonthermal, weak (0.6–307 sfu) narrow-band (4–5 MHz), short-lived (1–2 s) bursts. This figure has been constructed with data presented in Suresh et al. (2017).

8.1. Electron acceleration

Flare energy release and particle acceleration appear to be spatially fragmented processes, where the acceleration region may not coincide with the region of magnetic energy release (e.g. see the reviews by Bastian and Vlahos, 1997; Zharkova et al., 2011). Furthermore, the energy partition (Emslie et al., 2012; Aschwanden et al., 2017) and the efficiency of the particle acceleration may vary from event to event, from purely thermal (e.g. Gary and Hurford, 1989) to acceleration-dominated (e.g. Krucker et al., 2010; Fleishman et al., 2011).

The high sensitivity of radio emission to nonthermal electrons makes it possible to probe rather tenuous electron acceleration sites that could not be detected by hard X-rays which require higher densities as observed in some events (Xu et al., 2008; Kontar et al., 2011). Radio diagnostics of the electron acceleration region include (1) decimetric type III bursts, (2) decimetric narrow-band spikes, and (3) microwave narrow-band gyrosynchrotron bursts.

Type III bursts are plasma emissions resulted from the propagation of beams of energetic electrons along open field lines (see Suzuki and Dulk, 1985; Reid and Ratcliffe, 2014, for reviews). Of particular interest are the decimetric type III bursts that usually (but not always) occur in the 400 MHz to 1 GHz frequency range which corresponds to densities of $2–12 \times 10^9$ cm^{-3}; i.e. to the heights where flare energy release occurs (e.g. Benz, 2004). Reid et al. (2011, 2014) combined hard X-ray spectroscopic data and radio dynamic spectra of type III bursts to find that the acceleration region is located well above soft X-ray flaring loop tops at heights between 25 and 200 Mm. This result is consistent with earlier findings by Aschwanden and Benz (1997).

The potential of exploiting decimetric and metric type III bursts for the diagnosis of the electron acceleration site is hampered by the fact that relevant multi-frequency imaging observations are rare and only at a few discrete frequencies (e.g. Aurass and Klein, 1997; Paesold et al., 2001; Alissandrakis et al., 2015). Probably the only imaging spectroscopic observation of a type III burst has been reported by Chen et al. (2013) who found that the radio data indicated that the energy release showed fragmentation in space and time, suggesting a bursty reconnection scenario.

Among the coherent transient emissions at decimetric wavelengths, spikes are expected to show the closest relation to the electron acceleration region because (1) they show the highest correlation with hard X-rays (e.g. Benz, 1986; Aschwanden and Guedel, 1992) and (2) they occur at the rise phase of the flare (Slottje, 1978). However, studies of the locations of decimetric spike bursts and hard X-ray sources suggest the presence of a secondary acceleration region high up in the corona, away from the flaring site (Benz et al., 2002; Khan and Aurass, 2006; Battaglia and Benz, 2009).

Fleishman et al. (2011, 2013, 2016) have shown that narrow-band microwave gyrosynchrotron radiation which is emitted directly from the acceleration region can be detected when the trapped electron population is negligible. This emission distinguishes itself from the usual broadband gyrosynchrotron emission due to the steep energy spectrum of electrons accelerated in a rather uniform source.

8.2. Electron transport

Electron transport during flares is usually discussed in relation to the dynamics of both the radio and associated hard X-ray emission. The most widely used model is the "direct precipitation/trap plus precipitation" (DP/TPP) model (e.g. see Bastian et al., 1998; Aschwanden, 2002, as reviews). Briefly, the magnetic field guides accelerated electrons with small pitch angles to the chromosphere, where the dense plasma stops them (e.g. Holman et al., 2011, for a review). The largest part of their energy heats the ambient chromosphere while a smaller part is emitted in HXRs via the nonthermal "thick-target" free-free mechanism. Electrons with sufficiently large pitch angles are trapped in the flaring loop and produce gyrosynchrotron emission. Eventually, they are scattered into the loss cone through wave-particle interactions or Coulomb collisions and precipitate into the chromosphere, producing additional hard X-ray emission. Microwave gyrosynchrotron emission does not come exclusively from trapped electrons; in several studies microwave emission has been reported from the precipitating electrons (e.g. Kundu et al., 2001b; Lee et al., 2002) or from electrons that are efficiently scattered (Musset et al., 2018).

The observed signatures of gyrosynchrotron radiation are sensitive to anisotropies in the electron distribution function (e.g. Lee and Gary, 2000). However, it is not always straightforward to deduce whether the anisotropies stem from the injection/acceleration of the electrons or from transport effects (e.g. Melnikov et al., 2002) and it appears that acceleration and transport are interwined in some cases (e.g. Bastian et al., 2007).

8.3. Magnetic field diagnostics in flaring loops

The spectral and spatial structure of microwave gyrosynchrotron emission from flaring loops has a strong dependence on the magnetic field and the properties of energetic electrons. The spectral peak divides the spectrum into an optically thick low frequency part and an optically thin high frequency part. In a flaring loop the magnetic field is strongest near the footpoints and decreases toward the loop top. Therefore, at a given frequency the higher the energy of the electrons, the closer to the flaring loop top will they emit. Consequently, for a homogeneous isotropic distribution of energetic electrons, at high frequencies we expect to obtain optically thin emission primarily from the footpoints of the flaring loop (e.g. Alissandrakis

et al., 1993) while more extended optically thick sources should appear with the decrease of the frequency of observation (e.g. Wang et al., 1994). Anisotropies or/and inhomogeneities in the properties of the electrons may modify the above picture, for example by the development of optically thin loop top sources due to high concentration of energetic electrons there (Melnikov et al., 2002) (see also Kundu et al., 2001a; White et al., 2002; Tzatzakis et al., 2008). An example of the diversity of gyrosynchrotron source morphologies is presented in Fig. 6.

The above discussion indicates that the use of gyrosynchrotron emission for diagnostics of the magnetic field is not as straightforward as in the case of gyroresonance. For reliable diagnostics one would need to combine detailed modeling of the gyrosynchrotron emission (e.g. Klein and Trottet, 1984; Alissandrakis and Preka-Papadema, 1984; Bastian et al., 1998; Fleishman and Kuznetsov, 2010; Simões and Costa, 2010; Kuznetsov et al., 2011; Nita et al., 2015) with spectroscopic imaging observations. Thus any information on the magnetic field comes as a result of modeling. In spite of the difficulties, modeling of individual events observed either by the VLA and OVSA (Nindos et al., 2000b) or by the NoRH and the Nobeyama Polarimeter (e.g. Kundu et al., 2004; Tzatzakis et al., 2008; Kuznetsov and Kontar, 2015) have yielded magnetic field strengths ranging between 1700 G at the footpoints and 200 G at the loop top.

8.4. SKA's contribution to flare research

The discussion in Sections 8.1–8.3 indicates that despite the significant recent progress, several fundamental questions about the physics of flares remain unanswered. These questions include: (1) The location of electron acceleration, its magnetic configuration, and its relation to the site of energy release. (2) The mechanism(s) responsible for electron acceleration and the conditions under which they operate. Several acceleration models have been proposed (e.g. see Zharkova et al., 2011; Klein and Dalla, 2017, for reviews) but all of them are in need of reliable observational inputs. (3) The accurate determination of the distribution function of the energetic electrons and its evolution in space and time. (4) The factors that determine the efficiency with which magnetic energy is converted into energy of nonthermal particles. (5) The physical processes responsible for the transport of accelerated electrons and how one can disentangle injection/acceleration from transport effects.

The unique capabilities of SKA1 have the potential to provide significant advances in addressing the above questions. First of all, SKA1 will provide the means to perform coronal magnetic field measurements before, during, and after flares (see Section 6), thus allowing the determination of the magnetic free energy that becomes available. The relevant results will be superior from the ones provided by nonlinear force-free extrapolations of the photospheric field because the latter provide non-unique solutions (e.g. De Rosa et al., 2009), rely on field measurements in layers where the field is not force-free (Metcalf et al., 1995) and their cadence is not sufficient to capture the impulsive evolution of energy release and particle acceleration. Spectroscopic imaging observations will allow to establish the location of electron acceleration and to provide important constrains on the relevant acceleration mechanisms by revealing, in unprecedented detail, the properties of the bursts that are believed to be intimately related to the acceleration process, and most probably by discovering new relevant diagnostics. The combination of forward fitting

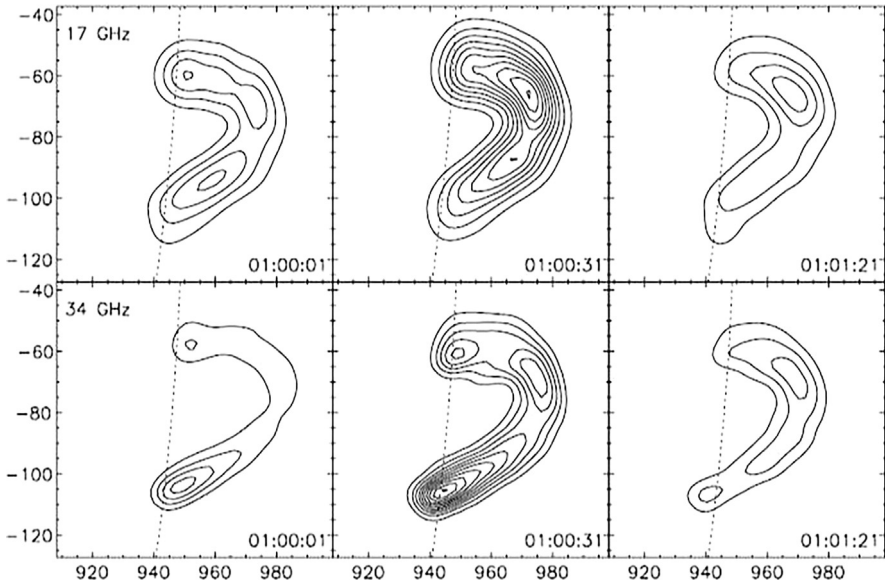

Fig. 6. A large flaring loop observed at 17 and 34 GHz with the NoRH. Contours are at 10% intervals of 550 and 170×10^6 K at 17 and 34 GHz, respectively. From Tzatzakis et al. (2008). Reproduced with permission ©Springer Nature.

techniques with high-cadence spatially resolved spectra of the gyrosynchrotron emission will allow to constrain both the properties of the electron distribution function and the magnetic field in the flaring volume more accurately than ever before.

9. Large-scale transient activity and space weather

9.1. Coronal mass ejections

All CME constituents emit radio radiation (see Gopalswamy, 2011, for a review). Eruptive prominences that later will evolve into the cores of white-light CMEs are observed at microwaves via the thermal optically thick free-free emission that they emit (e.g. Hanaoka et al., 1994; Gopalswamy et al., 1996, 2003; Grechnev et al., 2006; Gopalswamy and Yashiro, 2013). These observations complement the usual Hα observations and have the advantage that the continuum free-free emission can be detected even when the material is heated to high temperatures that make it undetectable in Hα. Higher up, one anticipates production of optically thin free-free emission from the whole CME that could be detected at lower frequencies. However such observations are rather rare (e.g. Sheridan, 1978; Gopalswamy and Kundu, 1992; Kathiravan et al., 2002; Ramesh et al., 2003) because the relevant emission is weak (due to the high temperatures and low densities that usually prevail in CMEs) and often outshined by the stronger nonthermal emissions. When detected, the free-free emission from CMEs provides an alternative way to estimate their masses (Gopalswamy and Kundu, 1992).

At radio dynamic spectra, CME-related emissions include type II bursts (see Section 9.2) as well as stationary and moving type IV bursts. The stationary type IV bursts emanate from electrons trapped in post-eruption arcades behind CMEs while the moving ones correspond to CME-related outward-moving material. Stationary type IV bursts should arise from plasma emission mechanism, while plasma emission (e.g. Duncan, 1981; Stewart et al., 1982; Gopalswamy and Kundu, 1989; Klein and Mouradian, 2002; Ramesh et al., 2013; Hariharan et al., 2016), and more rarely gyrosynchrotron emission from nonthermal electrons (Gopalswamy and Kundu, 1987; Bastian et al., 2001; Maia et al., 2007; Tun and Vourlidas, 2013; Bain et al., 2014; Carley et al., 2017) have been invoked for the interpretation of the properties of moving type IV bursts. The detection of gyrosynchrotron emission from some CMEs (see Fig. 7 for an example), is important because, if combined with modeling (see Section 8.3), it could provide estimates about the CME magnetic field; in the publications cited above, CME magnetic fields from 15 to 0.1 G have been reported at heights from $1.3R_\odot$ to $2.8R_\odot$.

Radio imaging observations of the early development of CMEs, albeit at few frequencies only, have revealed a large diversity of magnetic configurations that produce energetic electrons (e.g. Klein et al., 2001; Pohjolainen et al., 2001; Maia et al., 2003; Pick et al., 2005a, 2006; Démoulin et al., 2012; Carley et al., 2016). Such observations are a necessary ingredient for any validation of CME initiation models because nonthermal radio emissions could highlight possible locations of magnetic reconnection.

The potential of radio observations to CME research has not been fully exploited because of their lack of spectroscopic imaging capabilities and their inadequate sensitivity. SKA1 capabilities promise to change that situation. First of all, SKA1's high angular, spectral, and temporal resolution will provide, for the first time, a comprehensive picture of CMEs over extended frequency ranges. Since plasma emission probes the plasma frequency level or/and its second harmonic the resulted radio morphologies may be different from the white-light CME morphologies, therefore for non-incremental progress, one should be able to image both the thermal free-free emission

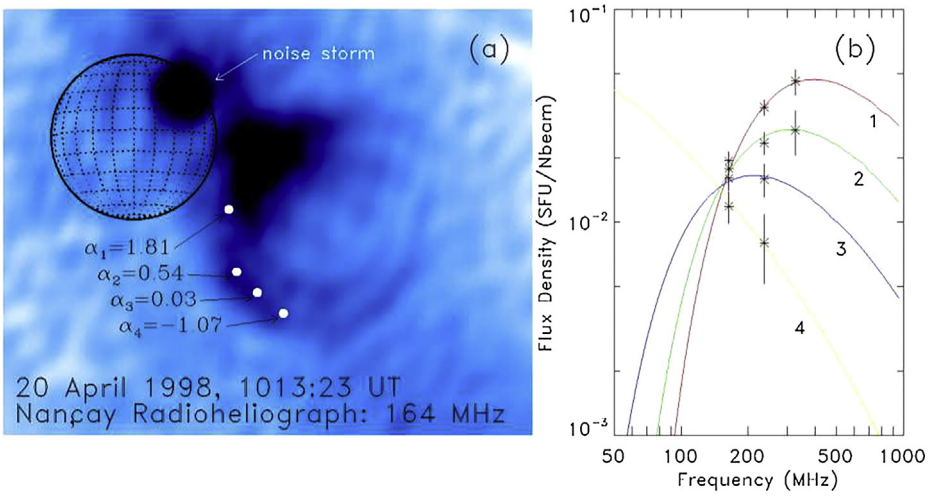

Fig. 7. (a) Image of a CME at 164 MHz computed from NRH data. The spectral index estimated at the locations of the four white dots is also marked. (b) Flux spectra estimated at the points marked in (a) accompanied by model gyrosynchrotron spectra. From Bastian et al. (2001). Reproduced by permission of the AAS.

and the much stronger plasma emission simultaneously. For this task a dynamic range of at least 10^4 is required (see the discussion in Section 4) which should be well within SKA1's capabilities. We also note that according to Bastian and Gary (1997) the optimum frequency range for the detection of free-free emission from CMEs is between 0.2 and 2 GHz (i.e. within SKA1's frequency range).

SKA1-LOW will be ideal to probe the early development of CMEs (including earth-directed ones whose detection by coronagraphs at L1 might be difficult at times), study the flare-CME relationship, and determine the sites of CME-related electron acceleration. SKA1-LOW's wide field of view will allow to study the effects of CMEs on the surrounding plasma and their evolution into interplanetary disturbances. Finally, the spectroscopic imaging capabilities of the instrument combined with its high sensitivity also promise more frequent detections of gyrosynchrotron emission from CMEs, and consequently the development of a statistically significant sample of CME magnetic field estimates.

SKA1 will also play a key role in studying CMEs in the interplanetary medium. Along with the more traditional interplanetary scintillation studies, heliospheric science with the SKA is also expected to include studies of the Faraday rotation of linearly polarized background radiation due to the magnetized solar wind and CME plasma. In this article we restrict ourselves only to a discussion of the solar physics questions which can be addressed with the SKA1. While important and interesting, the heliospheric physics to be pursued by the SKA1 lies outside the scope of this article. Interested readers are referred to the review by Nakariakov et al. (2015) for a short discussion of these topics.

9.2. Coronal shocks

Type II bursts are plasma emissions resulting from the propagation of MHD shocks in the corona; the emission appears as narrow-band lanes at the plasma frequency or/and its second harmonic (see the reviews by Nelson and Melrose, 1985; Vršnak and Cliver, 2008; Pick and Vilmer, 2008; Nindos et al., 2008). Although interplanetary type II bursts are generated exclusively by CME-driven shocks (Gopalswamy, 2006), the combination of radio imaging observations with coronagraphic, EUV, and soft X-ray data show that coronal shocks could appear close to either the leading edge (e.g. Maia et al., 2000; Ramesh et al., 2012) or the flanks of CMEs (e.g. Cho et al., 2007; Zucca et al., 2014a), ahead of erupting flux ropes (Bain et al., 2012; Zimovets and Sadykov, 2015, see Fig. 8), above expanding loops (Klein et al., 1999b; Dauphin et al., 2006), in conjunction with jets that erupt in the course of CMEs (Zucca et al., 2014b), and ahead of EUV bubbles (Kouloumvakos et al., 2014). CME deflections (Pick et al., 2016) and streamer-CME interactions (Kong et al., 2012; Eselevich et al., 2015) in the low corona could also play a role in the generation of coronal shocks. Some coronal shocks are flare-related (Magdalenić et al., 2008, 2010, 2012; Nindos et al., 2011; Kumar et al., 2016) because either there was no CME or the timing of the CME did not match the timing of the type II burst.

The above discussion indicates that coronal shocks could be produced by a variety of drivers: CMEs, small-scale ejecta associated with flares or flare pressure pulses. Some authors (e.g. Gopalswamy et al., 2005, 2009) have concluded that all metric type II bursts are generated by CME-driven shocks and the popularity of this interpretation is reinforced by the high association between metric

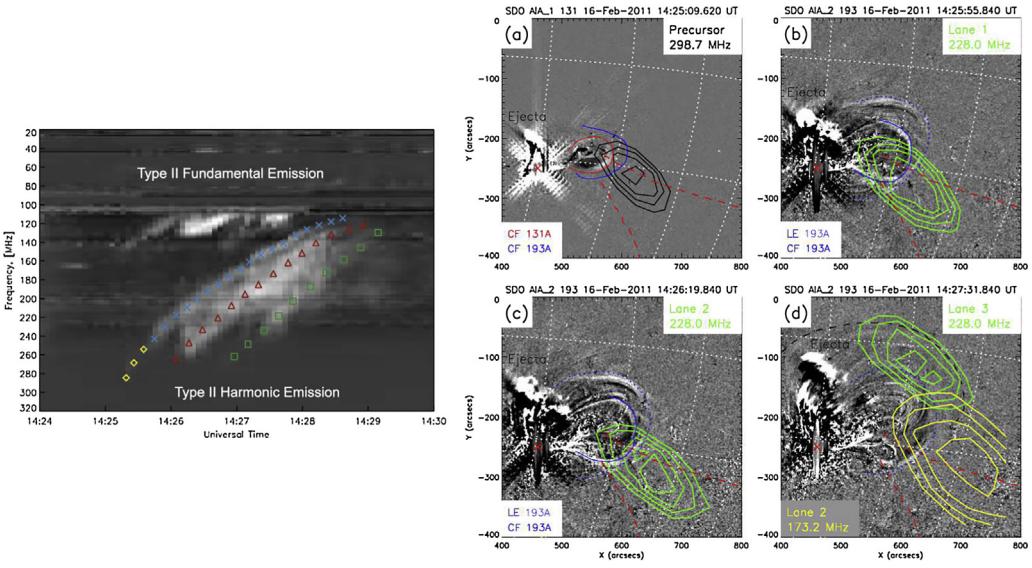

Fig. 8. Left: a complex type II burst observed by the ARTEMIS IV radio spectrograph. Yellow diamonds mark precursor activity while the blue, red, and green symbols mark the central frequencies of the three emission lanes of the harmonic emission. Right: Contour plots of precursor (a) and type II (b-d) second harmonic emission of the event in the ARTEMIS dynamic spectrum. The background consists of AIA 131 Å difference images. After Zimovets and Sadykov (2015). Reproduced with permission ©Elsevier.

type II bursts and EUV waves, the latter being driven by the lateral expansion of CMEs (e.g. Patsourakos and Vourlidas, 2012). However, it is fair to say that for a few events a flare origin cannot be excluded.

Progress in the study of coronal shocks has been limited by the inadequate angular and spectral resolution as well as sensitivity of radio imaging instruments and by the fact that the coronal shock emission that they detect may come from heights occulted in coronagraphs. SKA1-LOW's specifications promise significant advances in our understanding of coronal shocks. With its superior angular-spectral resolution and dynamic range, the instrument will be able to image both the CME and shock radio emission simultaneously which (combined with observations in the EUV and soft X-rays) will help us identify unambiguously the role of each eruption constituent to the development of the shock from its earliest stages. SKA1-LOW's wide field of view will also help us monitor the shock propagation and evolution in the corona, well above the heights obscured by the occulting disk of coronagraphs. Furthermore, the fine structure of type II bursts (e.g. Mann and Klassen, 2005; Carley et al., 2013; Mann et al., 2018) will be recorded with unprecedented detail which is an essential step to constrain shock inhomogeneities and turbulence as well as the role of shocks in particle acceleration.

9.3. Origin of solar energetic particles

Solar energetic particle (SEP) events are important for both the study of particle acceleration and space weather (e.g. Reames, 1999; Gopalswamy et al., 2008; Vainio et al., 2009; Valtonen, 2011). Since the work by Reames (1999) SEP events are usually classified into two groups: impulsive or gradual depending on the strength and duration of the parent soft X-ray flare, their association with type III or type II/IV bursts, charge states and abundances of the energetic particles, and the absence or presence of a CME. Impulsive events is thought to originate from particle acceleration induced by flare-related magnetic reconnection while the acceleration of gradual-event particles is thought to originate from CME-driven interplanetary or/and coronal shocks.

The above dichotomy has been challenged by several particle and radio/hard X-ray studies (e.g. Klein et al., 1999a, 2014; Laitinen et al., 2000; Klein and Trottet, 2001; Cane et al., 2002; Klein and Posner, 2005; Kouloumvakos et al., 2015) which indicate that it is difficult to establish a clear distinction between CME-associated and flare-associated SEP events. After all, reconnection, for example, could occur not only during the impulsive phase of flares but also in current sheets that are formed behind CMEs while acceleration by shocks generated by the interaction of reconnection outflows with loops in a cusp-shaped configuration might also be possible (e.g. Aurass et al., 2002; Aurass and Mann, 2004; Mann et al., 2009; Warmuth et al., 2009; Chen et al., 2013).

Sections 8 and 9.1–9.2 indicate that SKA will probe in an unprecedented way the diverse agents of particle acceleration in the low and middle corona and therefore we expect that its observations will provide key inputs that will help shed light on the controversies related to the origin of SEPs.

10. Synergistic activities

SKA's construction overlaps with the operation and/or development of important new-generation ground-based and space-borne solar instruments.

Ground-based facilities include Big Bear Solar Observatory's Goode Solar Telescope (in operation since 2009; Goode and Cao, 2012), the Daniel K. Inouye Solar Telescope (Tritschler et al., 2015, under construction with a planned completion date of 2019) and the European Solar Telescope (Matthews et al., 2016, under construction with a planned completion date of 2020). These instruments observe (or could) observe the photosphere and chromosphere in optical or/and near-infrared wavelengths with unprecedented sensitivity (owing to their large apertures), angular resolution ($\sim 0.1''$ using adaptive optics), and polarization accuracy ($\sim 10^{-4}$ of intensity). Their science objectives include the study of (1) solar magnetic fields (their life cycle and their role in the initiation of transient activity), and (2) the mechanisms of solar variability. The SKA will not be able to observe the layers probed by the above instruments, but coordinated observations will be of major importance providing a comprehensive picture of all layers of the solar atmosphere, from the photosphere to the outer corona.

The most important forthcoming solar space missions are the Parker Solar Probe (PSP, Fox et al., 2016) and the Solar Orbiter (SO, Müller et al., 2013), which are scheduled for launch in 2018 and 2020, respectively. Both missions are designed to approach the Sun closer than ever before (10 and $60R_{\odot}$, correspondingly) and carry several instruments for in situ measurements. As for remote sensing instruments they will both be equipped with heliospheric imagers while SO will also be equipped with a vector magnetograph, instruments for EUV imaging and spectroscopy, a telescope/spectrometer for thermal and nonthermal X-ray emission, and a coronagraph. SKA1 and SO/PSP data will complement each other. For example, due to their close approach to the Sun both SO and SPP could measure SEP properties with minimal influence of transport effects, while SKA1 will provide information about energetic electron seed populations and the role of flares and CME-driven shocks in SEP acceleration. The combination of SKA observations with data from the in situ radio wave instruments (available from both SO and PSP) will allow to track (albeit spatially unresolved) CME-related emissions recorded by the SKA1 into the interplanetary medium. Measurements of the magnetic field in the lower solar atmosphere by SO will complement

the SKA1's coronal magnetography capabilities, while the combination of SKA1 data with SO hard X-ray observations could provide new opportunities to study flare electron acceleration low in the solar atmosphere. SO/PSP synergies with the SKA1 will also have a strong heliospheric component because SKA1 observations could provide constraints on turbulence and waves in the solar wind (see Nakariakov et al., 2015, for details). Finally, needless to say that coordinated observations between the SKA1 and currently existing space instruments (e.g. SDO, RHESSI, STEREO, Hinode, and IRIS) could also be very useful.

SKA1-LOW solar observations will overlap in time with solar-dedicated radio heliographs that will observe at higher frequencies (NoRH, MUSER, and Siberian RH). The temporal overlap could be exploited to partially compensate for the most probable inability to operate the SKA1-MID and LOW arrays simultaneously. The successful exploitation and interpretation of several SKA1 observations will benefit from recent developments in theory (e.g. Zharkova et al., 2011; Hannah et al., 2013; Kontar et al., 2015, 2017a) and simulations of solar radio emissions (e.g. Tsiklauri, 2011; Li and Cairns, 2012; Gordovskyy et al., 2014; Schmidt and Cairns, 2014; Ratcliffe et al., 2014; Schmidt and Cairns, 2016).

11. Summary

The SKA is a unique radio instrument which promises to transform practically all branches of astrophysics due to its unique specifications which, even after completion of the Phase 1 of its deployment (i.e. SKA1), could significantly outperform all other radio telescopes. Solar physics benefits immensely from the deployment of the SKA because of the feasibility of solar observations with both SKA1-LOW and SKA1-MID. SKA1's unprecedented angular, spectral, and temporal resolution, as well as sensitivity will provide major new insights into many important solar physics problems.

Observations of the non-flaring solar atmosphere will provide time series of its thermal state which can be checked against solar-atmosphere heating models. The detection of numerous weak transient events could facilitate the derivation of reliable estimates about their contribution to coronal heating in the framework of the nanoflare model.

Several radio emission mechanisms/processes are uniquely sensitive to magnetic field, and one of the most important outcomes of SKA1 observations will be the direct and indirect measurements of the magnetic field at heights unaccessible by other instruments. The measurements can be used both for the computations of magnetic free energy budgets as well as for the diagnosis of the magnetic field of active regions, flaring loops, and CMEs.

SKA1 observations have strong potential to provide a comprehensive view of coherent and incoherent emissions that are intimately related to electron acceleration, of gyrosynchrotron emission from precipitating and trapped electrons in flaring loops, as well as of CMEs, shocks, and related phenomena. These observations have the potential to provide major advances to key solar physics questions about: (1) the location and magnetic configuration of the electron acceleration site, (2) the mechanism(s) responsible for particle acceleration, (3) the flare-CME relationship, (4) the timing and evolution of CMEs from the early stages of development all the way to the outer corona, (5) the drivers of coronal shocks as well as the locations and efficiency of electron acceleration by shocks, and (6) the origin of SEPs.

Above all, as is always the case with new instruments that outperform their predecessors in a significant way, is the high probability of new discoveries that cannot be predicted now. This exciting prospect is further highlighted by the availability of synergistic activities between the SKA and the new generation of ground-based and space-borne solar instruments.

Acknowledgements

We acknowledge the activities of the members of the SHI SWG toward the goal to exploit SKA's capabilities for solar physics research. We thank the referees for their comments which led to improvement of the paper. EPK was supported by STFC consolidated grant ST/P000533/1. DO was partially supported by a grant from the Department of Atomic Energy, Government of India, for enabling Indian participation in the SKA.

References

Akhmedov, S.B., Borovik, V.N., Gelfreikh, G.B., et al., 1986. Structure of a solar active region from RATAN 600 and very large array observations. ApJ 301, 460–464. https://doi.org/10.1086/163914.

Alissandrakis, C.E., 1994. Radio observations of the quiet solar corona. Adv. Space Res. 14 (4), 81–91. https://doi.org/10.1016/0273-1177(94)90167-8.

Alissandrakis, C.E., Kundu, M.R., Lantos, P., 1980. A model for sunspot associated emission at 6 CM wavelength. A&A 82, 30–40.

Alissandrakis, C.E., Nindos, A., Kundu, M.R., 1993. Evidence for ordinary mode emission from microwave bursts. Sol. Phys. 147, 343–358. https://doi.org/10.1007/BF00690724.

Alissandrakis, C.E., Nindos, A., Patsourakos, S., et al., 2015. A tiny event producing an interplanetary type III burst. A&A 582, A52. https://doi.org/10.1051/0004-6361/201526265. Available from: <arXiv: 1507.08423>.

Alissandrakis, C.E., Preka-Papadema, P., 1984. Microwave emission and polarization of a flaring loop. A&A 139, 507–511.

Aschwanden, M.J., 2002. Particle acceleration and kinematics in solar flares - a synthesis of recent observations and theoretical concepts (invited review). Space Sci. Rev. 101, 1–227. https://doi.org/10.1023/A:1019712124366.

Aschwanden, M.J., Benz, A.O., 1997. Electron densities in solar flare loops, chromospheric evaporation upflows, and acceleration sites. ApJ 480, 825–839. https://doi.org/10.1086/303995.

Aschwanden, M.J., Caspi, A., Cohen, C.M.S., et al., 2017. Global energetics of solar flares. V. Energy closure in flares and coronal mass ejections. ApJ 836, 17. https://doi.org/10.3847/1538-4357/836/1/17. Available from: <arXiv:1701.01176>.

Aschwanden, M.J., Guedel, M., 1992. The coevolution of decimetric millisecond spikes and hard X-ray emission during solar flares. ApJ 401, 736–753. https://doi.org/10.1086/172101.

Aschwanden, M.J., Parnell, C.E., 2002. Nanoflare statistics from first principles: fractal geometry and temperature synthesis. ApJ 572, 1048–1071. https://doi.org/10.1086/340385.

Aschwanden, M.J., Tarbell, T.D., Nightingale, R.W., et al., 2000. Time variability of the "Quiet" Sun observed with TRACE. II. Physical parameters, temperature evolution, and energetics of extreme-ultraviolet nanoflares. ApJ 535, 1047–1065. https://doi.org/10.1086/308867.

Aurass, H., Klein, K.-L., 1997. Spectrographic and imaging observations of solar type U radio bursts. A&A Suppl. 123, 279–304. https://doi.org/10.1051/aas:1997161.

Aurass, H., Mann, G., 2004. Radio observation of electron acceleration at solar flare reconnection outflow termination shocks. ApJ 615, 526–530. https://doi.org/10.1086/424374.

Aurass, H., Vršnak, B., Mann, G., 2002. Shock-excited radio burst from reconnection outflow jet? A&A 384, 273–281. https://doi.org/10.1051/0004-6361:20011735.

Bain, H.M., Krucker, S., Glesener, L., Lin, R.P., 2012. Radio imaging of shock-accelerated electrons associated with an erupting plasmoid on 2010 November 3. ApJ 750, 44. https://doi.org/10.1088/0004-637X/750/1/44.

Bain, H.M., Krucker, S., Saint-Hilaire, P., Raftery, C.L., 2014. Radio imaging of a type IVM radio burst on the 14th of August 2010. ApJ 782, 43. https://doi.org/10.1088/0004-637X/782/1/43.

Bandiera, R., 1982. Diagnostic of coronal magnetic fields from microwave polarization reversal. A&A 112, 52–60.

Bastian, T.S., Benz, A.O., Gary, D.E., 1998. Radio emission from solar flares. ARA&A 36, 131–188. https://doi.org/10.1146/annurev.astro.36.1.131.

Bastian, T.S., Fleishman, G.D., Gary, D.E., 2007. Radio spectral evolution of an X-ray-poor impulsive solar flare: implications for plasma heating and electron acceleration. ApJ 666, 1256–1267. https://doi.org/10.1086/520106. Available from: <arXiv:0704.2413>.

Bastian, T.S., Gary, D.E., 1997. On the feasibility of imaging coronal mass ejections at radio wavelengths. JGR (Space) 102, 14031–14040. https://doi.org/10.1029/97JA00483.

Bastian, T.S., Pick, M., Kerdraon, A., et al., 2001. The coronal mass ejection of 1998 April 20: direct imaging at radio wavelengths. ApJ 558, L65–L69. https://doi.org/10.1086/323421.

Bastian, T.S., Vlahos, L., 1997. Energy release in the solar corona. In: Trottet, G. (Ed.), Coronal Physics from Radio and Space Observations, Lecture Notes in Physics, vol. 483. Springer Verlag, Berlin, pp. 68–90. https://doi.org/10.1007/BFb0106452.

Battaglia, M., Benz, A.O., 2009. Do solar decimetric spikes originate in coronal X-ray sources? A&A 499, L33–L36. https://doi.org/10.1051/0004-6361/200912143. Available from: <arXiv:0904.4146>.

Benz, A.O., 1986. Millisecond radio spikes. Sol. Phys. 104, 99–110. https://doi.org/10.1007/BF00159950.

Benz, A.O., 2004. Decimeter burst emission and particle acceleration. In: Gary, D.E., Keller, C.U. (Eds.), Astrophysics and Space Science Library, Astrophysics and Space Science Library, vol. 314, pp. 203–221. https://doi.org/10.1007/1-4020-2814-8_10.

Benz, A.O., 2009. Radio emission of the quiet Sun. In: Trümper, J. (Ed.), Landolt Börnstein. Springer-Verlag, Berlin, pp. 103–117. https://doi.org/10.1007/978-3-540-88055-4_5.

Benz, A.O., Krucker, S., 1999. Heating events in the quiet solar corona: multiwavelength correlations. A&A 341, 286–295.

Benz, A.O., Saint-Hilaire, P., Vilmer, N., 2002. Location of narrowband spikes in solar flares. A&A 383, 678–684. https://doi.org/10.1051/0004-6361:20011774. Available from: <arXiv:astro-ph/0112442>.

Bogod, V.M., Gelfreikh, G.B., 1980. Measurements of the magnetic field and the gradient of temperature in the solar atmosphere above a flocculus using radio observations. Sol. Phys. 67, 29–46. https://doi.org/10.1007/BF00146680.

Bowman, J.D., Cairns, I., Kaplan, D.L., et al., 2013. Science with the murchison widefield array. PASA 30, e031. https://doi.org/10.1017/pas.2013.009. Available from: <arXiv:1212.5151>.

Braun, R., Bourke, T., Green, J.A., et al., 2015. Advancing astrophysics with the square kilometre array. In: Bourke, T., Braun, R., Fender, R. (Eds.), Advancing Astrophysics with the Square Kilometre Array (AASKA14). Dolman Scott, Thatcham, pp. 3–11.

Cairns, I.H., Lobzin, V.V., Donea, A., et al., 2018. Low altitude solar magnetic reconnection, Type III solar radio bursts, and X-ray emissions. Sci. Rep. 8, 1676. https://doi.org/10.1038/s41598-018-19195-3.

Cane, H.V., Erickson, W.C., Prestage, N.P., 2002. Solar flares, type III radio bursts, coronal mass ejections, and energetic particles. J. Geophys. Res. (Space Phys.) 107, 1315. https://doi.org/10.1029/2001JA000320.

Carley, E.P., Long, D.M., Byrne, J.P., et al., 2013. Quasiperiodic acceleration of electrons by a plasmoid-driven shock in the solar atmosphere. Nat. Phys. 9, 811–816. https://doi.org/10.1038/nphys2767. Available from: <arXiv:1406.0743>.

Carley, E.P., Vilmer, N., Gallagher, P.T., 2016. Radio diagnostics of electron acceleration sites during the eruption of a flux rope in the solar corona. ApJ 833, 87. https://doi.org/10.3847/1538-4357/833/1/87. Available from: <arXiv:1609.01463>.

Carley, E.P., Vilmer, N., Simões, P.J.A., Ó Fearraigh, B., 2017. Estimation of a coronal mass ejection magnetic field strength using radio observations of gyrosynchrotron radiation. A&A 608, A137. https://doi.org/10.1051/0004-6361/201731368. Available from: <arXiv:1709.05184>.

Chen, B., Bastian, T.S., Shen, C., et al., 2015. Particle acceleration by a solar flare termination shock. Science 350, 1238–1242. https://doi.org/10.1126/science.aac8467. Available from: <arXiv:1512.02237>.

Chen, B., Bastian, T.S., White, S.M., et al., 2013. Tracing electron beams in the Sun's corona with radio dynamic imaging spectroscopy. ApJ 763, L21. https://doi.org/10.1088/2041-8205/763/1/L21. Available from: <arXiv:1211.3058>.

Chen, X., Kontar, E.P., Yu, S., et al., 2018. Fine structures of solar radio Type III bursts and their possible relationship with coronal density turbulence. ApJ 856, 73. https://doi.org/10.3847/1538-4357/aaa9bf. Available from: <arXiv:1801.07545>.

Cho, K.-S., Lee, J., Moon, Y.-J., et al., 2007. A study of CME and type II shock kinematics based on coronal density measurement. A&A 461, 1121–1125. https://doi.org/10.1051/0004-6361:20064920.

Dauphin, C., Vilmer, N., Krucker, S., 2006. Observations of a soft X-ray rising loop associated with a type II burst and a coronal mass ejection in the 03 November 2003 X-ray flare. A&A 455, 339–348. https://doi.org/10.1051/0004-6361:20054535.

De Moortel, I., Browning, P., 2015. Recent advances in coronal heating. Philosoph. Trans. Roy. Soc. Lond. Ser. A 373, 20140269. https://doi.org/10.1098/rsta.2014.0269. Available from: <arXiv:1510.00977>.

De Rosa, M.L., Schrijver, C.J., Barnes, G., et al., 2009. A critical assessment of nonlinear force-free field modeling of the solar corona for active region 10953. ApJ 696, 1780–1791. https://doi.org/10.1088/0004-637X/696/2/1780. Available from: <arXiv:0902.1007>.

Démoulin, P., Vourlidas, A., Pick, M., Bouteille, A., 2012. Initiation and development of the white-light and radio coronal mass ejection on 2001 April 15. ApJ 750, 147. https://doi.org/10.1088/0004-637X/750/2/147.

Dulk, G.A., 1985. Radio emission from the Sun and Stars. ARA&A 23, 169–224. https://doi.org/10.1146/annurev.aa.23.090185.001125.

Duncan, R.A., 1981. Langmuir-wave conversion as the explanation of moving type IV solar meter-wave radio outbursts. Sol. Phys. 73, 191–204. https://doi.org/10.1007/BF00153154.

Ellingson, S.W., Clarke, T.E., Cohen, A., et al., 2009. The long wavelength array. IEEE Proc. 97, 1421–1430. https://doi.org/10.1109/JPROC.2009.2015683.

Emslie, A.G., Dennis, B.R., Shih, A.Y., et al., 2012. Global energetics of thirty-eight large solar eruptive events. ApJ 759, 71. https://doi.org/10.1088/0004-637X/759/1/71. Available from: <arXiv:1209.2654>.

Eselevich, V.G., Eselevich, M.V., Sadykov, V.M., Zimovets, I.V., 2015. Evidence of a blast shock wave formation in a "CME-streamer" interaction. Adv. Space Res. 56, 2793–2803. https://doi.org/10.1016/j.asr.2015.03.041.

Fleishman, G.D., Kontar, E.P., Nita, G.M., Gary, D.E., 2011. A cold, tenuous solar flare: acceleration without heating. ApJ Lett. 731, L19. https://doi.org/10.1088/2041-8205/731/1/L19. Available from: <arXiv:1103.2705>.

Fleishman, G.D., Kontar, E.P., Nita, G.M., Gary, D.E., 2013. Probing dynamics of electron acceleration with radio and X-ray spectroscopy, imaging, and timing in the 2002 April 11 solar flare. ApJ 768, 190. https://doi.org/10.1088/0004-637X/768/2/190. Available from: <arXiv:1303.4098>.

Fleishman, G.D., Kuznetsov, A.A., 2010. Fast gyrosynchrotron codes. ApJ 721, 1127–1141. https://doi.org/10.1088/0004-637X/721/2/1127.

Fleishman, G.D., Melnikov, V.F., 2003a. Gyrosynchrotron emission from anisotropic electron distributions. ApJ 587, 823–835. https://doi.org/10.1086/368252.

Fleishman, G.D., Melnikov, V.F., 2003b. Optically thick gyrosynchrotron emission from anisotropic electron distributions. ApJ 584, 1071–1083. https://doi.org/10.1086/345849.

Fleishman, G.D., Nita, G.M., Kontar, E.P., Gary, D.E., 2016. Narrow-band gyrosynchrotron bursts: probing electron acceleration in solar flares. ApJ 826, 38. https://doi.org/10.3847/0004-637X/826/1/38. Available from: <arXiv:1605.00948>.

Fossum, A., Carlsson, M., 2005. High-frequency acoustic waves are not sufficient to heat the solar chromosphere. Nature 435, 919–921. https://doi.org/10.1038/nature03695.

Fox, N.J., Velli, M.C., Bale, S.D., et al., 2016. The solar probe plus mission: humanity's first visit to our star. Space Sci. Rev. 204, 7–48. https://doi.org/10.1007/s11214-015-0211-6.

Gary, D.E., 1999. Radio counterparts to SXR transients. In: Bastian, T.S., Gopalswamy, N., Shibasaki, K. (Eds.), Proceedings of the Nobeyama Symposium, vol. 479, pp. 129–134.

Gary, D.E., Hartl, M.D., Shimizu, T., 1997. Nonthermal radio emission from solar soft X-ray transient brightenings. ApJ 477, 958–968. https://doi.org/10.1086/303748.

Gary, D.E., Hurford, G.J., 1987. Multifrequency observations of a solar active region during a partial eclipse. ApJ 317, 522–533. https://doi.org/10.1086/165296.

Gary, D.E., Hurford, G.J., 1989. A simple solar microwave burst observed with high spectral resolution. ApJ 339, 1115–1122. https://doi.org/10.1086/167366.

Gary, D.E., Hurford, G.J., 1994. Coronal temperature, density, and magnetic field maps of a solar active region using the Owens Valley Solar Array. ApJ 420, 903–912. https://doi.org/10.1086/173614.

Gary, D.E., Nita, G.M., Sane, N., 2012. Expanded Owens Valley Solar Array (EOVSA) testbed and prototype. American Astronomical Society Meeting Abstracts #220, vol. 220. American Astronomical Society Meeting Abstracts, p. 204.30.

Goode, P.R., Cao, W., 2012. The 1.6 m off-axis New Solar Telescope (NST) in big bear. In: Second ATST-EAST Meeting: Magnetic Fields from the Photosphere to the Corona. In: Rimmele, T.R., Tritschler, A., Wöger, F., Collados Vera, M., Socas-Navarro, H., Schlichenmaier, R., Carlsson, M., Berger, T., Cadavid, A., Gilbert, P.R., Goode, P.R., Knölker, M. (Eds.), . Astronomical Society of the Pacific Conference Series, vol. 463, pp. 357–364.

Gopalswamy, N., 2006. Coronal mass ejections and type II radio bursts. In: Solar Eruptions and Energetic Particles. In: Gopalswamy, N., Mewaldt, R., Torsti, J. (Eds.), . Geophysical Monograph Series, vol. 165. American Geophysical Union, Washington DC, pp. 207–220. https://doi.org/10.1029/165GM20.

Gopalswamy, N., 2011. Coronal mass ejections and solar radio emissions. Planetary, Solar and Heliospheric Radio Emissions (PRE VII), 325–342.

Gopalswamy, N., Kundu, M.R., 1987. Simultaneous radio and white light observations of the 1984 June 27 coronal mass ejection event. Sol. Phys. 114, 347–362. https://doi.org/10.1007/BF00167350.

Gopalswamy, N., Kundu, M.R., 1989. Radioheliograph and white-light coronagraph studies of a coronal mass ejection event. Sol. Phys. 122, 145–173. https://doi.org/10.1007/BF00162832.

Gopalswamy, N., Kundu, M.R., 1992. Estimation of the mass of a coronal mass ejection from radio observations. ApJ Lett. 390, L37–L39. https://doi.org/10.1086/186366.

Gopalswamy, N., Kundu, M.R., Hanaoka, Y., et al., 1996. Yohkoh/SXT observations of a coronal mass ejection near the solar surface. New Astron. 1, 207–213. https://doi.org/10.1016/S1384-1076(96)00016-4.

Gopalswamy, N., Shimojo, M., Lu, W., Yashiro, S., Shibasaki, K., Howard, R.A., 2003. Prominence eruptions and coronal mass ejection: a statistical study using microwave observations. ApJ 586, 562–578. https://doi.org/10.1086/367614.

Gopalswamy, N., Aguilar-Rodriguez, E., Yashiro, S., et al., 2005. Type II radio bursts and energetic solar eruptions. JGR (Space) 110, A12S07. https://doi.org/10.1029/2005JA011158.

Gopalswamy, N., Thompson, W.T., Davila, J.M., et al., 2009. Relation between type II bursts and CMEs inferred from STEREO observations. Sol. Phys. 259, 227–254. https://doi.org/10.1007/s11207-009-9382-1.

Gopalswamy, N., Yashiro, S., 2013. Obscuration of flare emission by an eruptive prominence. PASJ 65, S11. https://doi.org/10.1093/pasj/65.sp1.S11. Available from: <arXiv:1309.2046>.

Gopalswamy, N., Yashiro, S., Akiyama, S., et al., 2008. Coronal mass ejections, type II radio bursts, and solar energetic particle events in the SOHO era. Ann. Geophys. 26, 3033–3047. https://doi.org/10.5194/angeo-26-3033-2008.

Gordovskyy, M., Browning, P.K., Kontar, E.P., Bian, N.H., 2014. Particle acceleration and transport in reconnecting twisted loops in a stratified atmosphere. A&A 561, A72. https://doi.org/10.1051/0004-6361/201321715. Available from: <arXiv:1501.06418>.

Grebinskij, A., Bogod, V., Gelfreikh, G., Urpo, S., Pohjolainen, S., Shibasaki, K., 2000. Microwave tomography of solar magnetic fields. A&A Suppl. 144, 169–180. https://doi.org/10.1051/aas:2000202.

Grechnev, V.V., Uralov, A.M., Zandanov, V.G., Baranov, N.Y., Shibasaki, K., 2006. Observations of prominence eruptions with two radioheliographs, SSRT, and NoRH. PASJ 58, 69–84. https://doi.org/10.1093/pasj/58.1.69.

Hall, P.J., 2005. The Square Kilometre Array: An Engineering Perspective. Springer, Dordrecht.

Hanaoka, Y., Kurokawa, H., Enome, S., et al., 1994. Simultaneous observations of a prominence eruption followed by a coronal arcade formation in radio, soft X-rays, and H(alpha). PASJ 46, 205–216.

Hannah, I.G., Kontar, E.P., Reid, H.A.S., 2013. Effect of turbulent density-fluctuations on wave-particle interactions and solar flare X-ray spectra. A&A 550, A51. https://doi.org/10.1051/0004-6361/201220462. Available from: <arXiv:1211.6015>.

Hariharan, K., Ramesh, R., Kathiravan, C., Wang, T.J., 2016. Simultaneous near-Sun observations of a moving Type IV radio burst and the associated white-light coronal mass ejection. Sol. Phys. 291, 1405–1416. https://doi.org/10.1007/s11207-016-0918-x.

Holman, G.D., Aschwanden, M.J., Aurass, H., et al., 2011. Implications of X-ray observations for electron acceleration and propagation in solar flares. Space Sci. Rev. 159, 107–166. https://doi.org/10.1007/s11214-010-9680-9. Available from: <arXiv:1109.6496>.

Kathiravan, C., Ramesh, R., Subramanian, K.R., 2002. Metric radio observations and ray-tracing analysis of the onset phase of a solar eruptive event. ApJ Lett. 567, L93–L95. https://doi.org/10.1086/339801.

Kerdraon, A., Delouis, J.-M., 1997. The Nançay Radioheliograph. In: Trottet, G. (Ed.), Coronal Physics from Radio and Space Observations, Lecture Notes in Physics, vol. 483. Springer Verlag, Berlin, pp. 192–201. https://doi.org/10.1007/BFb0106458.

Khan, J.I., Aurass, H., 2006. Observations of the coronal dynamics associated with solar radio spike burst emission. A&A 457, 319–328. https://doi.org/10.1051/0004-6361:20054034.

Klein, K.-L., Chupp, E.L., Trottet, G., et al., 1999a. Flare-associated energetic particles in the corona and at 1 AU. A&A 348, 271–285.

Klein, K.-L., Dalla, S., 2017. Acceleration and propagation of solar energetic particles. Space Sci. Rev. 212, 1107–1136. https://doi.org/10.1007/s11214-017-0382-4. Available from: <arXiv:1705.07274>.

Klein, K.-L., Khan, J.I., Vilmer, N., et al., 1999b. X-ray and radio evidence on the origin of a coronal shock wave. A&A 346, L53–L56.
Klein, K.-L., Masson, S., Bouratzis, C., et al., 2014. The relativistic solar particle event of 2005 January 20: origin of delayed particle acceleration. A&A 572, A4. https://doi.org/10.1051/0004-6361/201423783. Available from: <arXiv:1403.2260>.
Klein, K.-L., Mouradian, Z., 2002. The dynamics of an erupting prominence. A&A 381, 683–693. https://doi.org/10.1051/0004-6361:20011513.
Klein, K.-L., Posner, A., 2005. The onset of solar energetic particle events: prompt release of deka-MeV protons and associated coronal activity. A&A 438, 1029–1042. https://doi.org/10.1051/0004-6361:20042607.
Klein, K.-L., Trottet, G., 1984. Gyrosynchrotron radiation from a source with spatially varying field and density. A&A 141, 67–76.
Klein, K.-L., Trottet, G., 2001. The origin of solar energetic particle events: coronal acceleration versus shock wave acceleration. Space Sci. Rev. 95, 215–225.
Klein, K.-L., Trottet, G., Lantos, P., Delaboudinière, J.-P., 2001. Coronal electron acceleration and relativistic proton production during the 14 July 2000 flare and CME. A&A 373, 1073–1082. https://doi.org/10.1051/0004-6361:20010653.
Klimchuk, J.A., 2006. On solving the coronal heating problem. Sol. Phys. 234, 41–77. https://doi.org/10.1007/s11207-006-0055-z. Available from: <arXiv:astro-ph/0511841>.
Kong, X.L., Chen, Y., Li, G., et al., 2012. A broken solar Type II radio burst induced by a coronal shock propagating across the streamer boundary. ApJ 750, 158. https://doi.org/10.1088/0004-637X/750/2/158. Available from: <arXiv:1203.1511>.
Kontar, E.P., Hannah, I.G., Bian, N.H., 2011. Acceleration, magnetic fluctuations, and cross-field transport of energetic electrons in a solar flare loop. ApJ Lett. 730, L22. https://doi.org/10.1088/2041-8205/730/2/L22. Available from: <arXiv:1102.3664>.
Kontar, E.P., Jeffrey, N.L.S., Emslie, A.G., Bian, N.H., 2015. Collisional relaxation of electrons in a warm plasma and accelerated nonthermal electron spectra in solar flares. ApJ 809, 35. https://doi.org/10.1088/0004-637X/809/1/35. Available from: <arXiv:1505.03733>.
Kontar, E.P., Perez, J.E., Harra, L.K., et al., 2017a. Turbulent kinetic energy in the energy balance of a solar flare. Phys. Rev. Lett. 118, 155101. https://doi.org/10.1103/PhysRevLett.118.155101. Available from: <arXiv:1703.02392>.
Kontar, E.P., Yu, S., Kuznetsov, A.A., et al., 2017b. Imaging spectroscopy of solar radio burst fine structures. Nat. Commun. 8, 1515. https://doi.org/10.1038/s41467-017-01307-8. Available from: <arXiv:1708.06505>.
Kooi, J.E., Fischer, P.D., Buffo, J.J., Spangler, S.R., 2014. Measurements of coronal faraday rotation at 4.6 $R_\odot$. ApJ 784, 68. https://doi.org/10.1088/0004-637X/784/1/68. Available from: <arXiv:1307.1727>.
Korzhavin, A.N., Opeikina, L.V., Peterova, N.G., 2010. Transition region above sunspots inferred from microwave observations. Astrophys. Bull. 65, 60–74. https://doi.org/10.1134/S1990341310010062.
Kouloumvakos, A., Nindos, A., Valtonen, E., et al., 2015. Properties of solar energetic particle events inferred from their associated radio emission. A&A 580, A80. https://doi.org/10.1051/0004-6361/201424397. Available from: <arXiv:1507.03776>.
Kouloumvakos, A., Patsourakos, S., Hillaris, A., et al., 2014. CME expansion as the driver of metric Type II shock emission as revealed by self-consistent analysis of high-cadence EUV images and radio spectrograms. Sol. Phys. 289, 2123–2139. https://doi.org/10.1007/s11207-013-0460-z. Available from: <arXiv:1311.5159>.
Krucker, S., Benz, A.O., Bastian, T.S., Acton, L.W., 1997. X-ray network flares of the quiet Sun. ApJ 488, 499–505. https://doi.org/10.1086/304686.
Krucker, S., Hudson, H.S., Glesener, L., et al., 2010. Measurements of the coronal acceleration region of a solar flare. ApJ 714, 1108–1119. https://doi.org/10.1088/0004-637X/714/2/1108.
Kumar, P., Innes, D.E., Cho, K.-S., 2016. Flare-generated shock wave propagation through solar coronal arcade loops and an associated Type II radio burst. ApJ 828, 28. https://doi.org/10.3847/0004-637X/828/1/28. Available from: <arXiv:1606.05056>.
Kundu, M.R., Alissandrakis, C.E., 1984. Structure and polarization of active region microwave emission. Sol. Phys. 94, 249–283. https://doi.org/10.1007/BF00151317.
Kundu, M.R., Gergely, T.E., Szabo, A., et al., 1986. Solar microbursts at meter-dekameter wavelengths. ApJ 308, 436–442. https://doi.org/10.1086/164513.
Kundu, M.R., Nindos, A., Grechnev, V.V., 2004. The configuration of simple short-duration solar microwave bursts. A&A 420, 351–359. https://doi.org/10.1051/0004-6361:20034461.
Kundu, M.R., Nindos, A., White, S.M., Grechnev, V.V., 2001a. A multiwavelength study of three solar flares. ApJ 557, 880–890. https://doi.org/10.1086/321534.
Kundu, M.R., White, S.M., Shibasaki, K., et al., 2001b. Spatial structure of simple spiky bursts at microwave/millimeter wavelengths. ApJ 547, 1090–1099. https://doi.org/10.1086/318422.
Kuznetsov, A.A., Kontar, E.P., 2015. Spatially resolved energetic electron properties for the 21 May 2004 flare from radio observations and 3D simulations. Sol. Phys. 290, 79–93. https://doi.org/10.1007/s11207-014-0530-x. Available from: <arXiv:1403.5751>.
Kuznetsov, A.A., Nita, G.M., Fleishman, G.D., 2011. Three-dimensional simulations of gyrosynchrotron emission from mildly anisotropic nonuniform electron distributions in symmetric magnetic loops. ApJ 742, 87. https://doi.org/10.1088/0004-637X/742/2/87. Available from: <arXiv:1108.5150>.
Laitinen, T., Klein, K.-L., Kocharov, L., Torsti, J., Trottet, G., Bothmer, V., Kaiser, M.L., Rank, G., Reiner, M.J., 2000. Solar energetic particle event and radio bursts associated with the 1996 July 9 flare and coronal mass ejection. A&A 360, 729–741.
Lee, J., 2007. Radio emissions from solar active regions. Space Sci. Rev. 133, 73–102. https://doi.org/10.1007/s11214-007-9206-2.
Lee, J., Gary, D.E., 2000. Solar microwave bursts and injection pitch-angle distribution of flare electrons. ApJ 543, 457–471. https://doi.org/10.1086/317080.
Lee, J., Gary, D.E., Qiu, J., Gallagher, P.T., 2002. Electron transport during the 1999 August 20 flare inferred from microwave and hard X-ray observations. ApJ 572, 609–625. https://doi.org/10.1086/340311.
Lesovoi, S.V., Altyntsev, A.T., Ivanov, E.F., Gubin, A.V., 2014. A 96-antenna radioheliograph. Res. Astron. Astrophys. 14, 864–868. https://doi.org/10.1088/1674-4527/14/7/008. Available from: <arXiv:1403.4748>.
Li, B., Cairns, I.H., 2012. Type III radio bursts perturbed by weak coronal shocks. ApJ 753, 124. https://doi.org/10.1088/0004-637X/753/2/124.
Lin, H., Kuhn, J.R., Coulter, R., 2004. Coronal magnetic field measurements. ApJ Lett. 613, L177–L180. https://doi.org/10.1086/425217.
Lin, R.P., Schwartz, R.A., Kane, S.R., et al., 1984. Solar hard X-ray microflares. ApJ 283, 421–425. https://doi.org/10.1086/162321.
Magdalenić, J., Marqué, C., Zhukov, A.N., et al., 2010. Origin of coronal shock waves associated with slow coronal mass ejections. ApJ 718, 266–278. https://doi.org/10.1088/0004-637X/718/1/266.
Magdalenić, J., Marqué, C., Zhukov, A.N., et al., 2012. Flare-generated Type II burst without associated coronal mass ejection. ApJ 746, 152. https://doi.org/10.1088/0004-637X/746/2/152.
Magdalenić, J., Vršnak, B., Pohjolainen, S., et al., 2008. A flare-generated shock during a coronal mass ejection on 24 December 1996. Sol. Phys. 253, 305–317. https://doi.org/10.1007/s11207-008-9220-x.
Maia, D., Aulanier, G., Wang, S.J., et al., 2003. Interpretation of a complex CME event: coupling of scales in multiple flux systems. A&A 405, 313–323. https://doi.org/10.1051/0004-6361:20030359.
Maia, D., Pick, M., Vourlidas, A., Howard, R., 2000. Development of coronal mass ejections: radio shock signatures. ApJ Lett. 528, L49–L51. https://doi.org/10.1086/312421.
Maia, D.J.F., Gama, R., Mercier, C., Pick, M., Kerdraon, A., Karlický, M., 2007. The radio-coronal mass ejection event on 2001 April 15. ApJ 660, 874–881. https://doi.org/10.1086/508011.
Mann, G., Klassen, A., 2005. Electron beams generated by shock waves in the solar corona. A&A 441, 319–326. https://doi.org/10.1051/0004-6361:20034396.

Mann, G., Melnik, V.N., Rucker, H.O., et al., 2018. Radio signatures of shock-accelerated electron beams in the solar corona. A&A 609, A41. https://doi.org/10.1051/0004-6361/201730546.

Mann, G., Warmuth, A., Aurass, H., 2009. Generation of highly energetic electrons at reconnection outflow shocks during solar flares. A&A 494, 669–675. https://doi.org/10.1051/0004-6361:200810099.

Matthews, S.A., Collados, M., Mathioudakis, M., Erdelyi, R., 2016. The European Solar Telescope (EST). In: Ground-based and Airborne Instrumentation for Astronomy VI. Proc. SPIE, vol. 9908, p. 990809. https://doi.org/10.1117/12.2234145.

McCauley, P.I., Cairns, I.H., Morgan, J., et al., 2017. Type III solar radio burst source region splitting due to a quasi-separatrix layer. ApJ 851, 151. https://doi.org/10.3847/1538-4357/aa9cee. Available from: <arXiv:1711.04930>.

Melnikov, V.F., Shibasaki, K., Reznikova, V.E., 2002. Loop-top nonthermal microwave source in extended solar flaring loops. ApJ Lett. 580, L185–L188. https://doi.org/10.1086/345587.

Melrose, D.B., 1980. Plasma astrophysics: nonthermal processes in diffuse magnetized plasmas. Astrophysical Applications, vol. 2. Gordon and Breach, New York.

Mercier, C., Chambe, G., 2009. High dynamic range images of the solar corona between 150 and 450 MHz. ApJ Lett. 700, L137–L140. https://doi.org/10.1088/0004-637X/700/2/L137.

Metcalf, T.R., Jiao, L., McClymont, A.N., Canfield, R.C., Uitenbroek, H., 1995. Is the solar chromospheric magnetic field force-free? ApJ 439, 474–481. https://doi.org/10.1086/175188.

Mohan, A., Oberoi, D., 2017. 4D data cubes from radio-interferometric spectroscopic snapshot imaging. Sol. Phys. 292, 168. https://doi.org/10.1007/s11207-017-1193-1. Available from: <arXiv:1710.10525>.

Mondal, S., Mohan, A., Oberoi, D., et al., 2018. A novel algorithm for unsupervised self-calibration of solar interferometric data. ApJ 110, submitted for publication.

Morosan, D.E., Gallagher, P.T., Fallows, R.A., et al., 2017. The association of a J-burst with a solar jet. A&A 606, A81. https://doi.org/10.1051/0004-6361/201629996. Available from: <arXiv:1707.03428>.

Morosan, D.E., Gallagher, P.T., Zucca, P., et al., 2014. LOFAR tied-array imaging of Type III solar radio bursts. A&A 568, A67. https://doi.org/10.1051/0004-6361/201423936. Available from: <arXiv:1407.4385>.

Morosan, D.E., Gallagher, P.T., Zucca, P., et al., 2015. LOFAR tied-array imaging and spectroscopy of solar S bursts. A&A 580, A65. https://doi.org/10.1051/0004-6361/201526064. Available from: <arXiv:1507.07496>.

Müller, D., Marsden, R.G., St. Cyr, O.C., Gilbert, H.R., 2013. Solar orbiter. Exploring the Sun-heliosphere connection. Sol. Phys. 285, 25–70. https://doi.org/10.1007/s11207-012-0085-7. Available from: <arXiv:1207.4579>.

Musset, S., Kontar, E.P., Vilmer, N., 2018. Diffusive transport of energetic electrons in the solar corona: X-ray and radio diagnostics. A&A 610, A6. https://doi.org/10.1051/0004-6361/201731514. Available from: <arXiv:1710.00765>.

Nakajima, H., Nishio, M., Enome, S., et al., 1994. The Nobeyama radioheliograph. IEEE Proc. 82, 705–713.

Nakariakov, V., Bisi, M.M., Browning, P.K., et al., 2015. Solar and heliospheric physics with the square kilometre array. In: Bourke, T., Braun, R., Fender, R. (Eds.), Advancing Astrophysics with the Square Kilometre Array (AASKA14). Dolman Scott, Thatcham, pp. 1875–1888. Available from: <arXiv:1507.00516>.

Nelson, G.J., Melrose, D.B., 1985. Type II bursts. In: McLean, D.J., Labrum, N.R. (Eds.), Solar Radiophysics: Studies of Emission from the Sun at Metre Wavelengths. Cambridge University Press, Cambridge, pp. 333–359.

Nindos, A., Alissandrakis, C.E., Hillaris, A., Preka-Papadema, P., 2011. On the relationship of shock waves to flares and coronal mass ejections. A&A 531, A31. https://doi.org/10.1051/0004-6361/201116799. Available from: <arXiv:1105.1268>.

Nindos, A., Aurass, H., Klein, K.-L., Trottet, G., 2008. Radio emission of flares and coronal mass ejections. Invited review. Sol. Phys. 253, 3–41. https://doi.org/10.1007/s11207-008-9258-9.

Nindos, A., Kundu, M.R., White, S.M., 1999. A study of microwave-selected coronal transient brightenings. ApJ 513, 983–989. https://doi.org/10.1086/306886.

Nindos, A., Kundu, M.R., White, S.M., et al., 2000a. Soft X-ray and gyroresonance emission above sunspots. ApJ Suppl. 130, 485–499. https://doi.org/10.1086/317355.

Nindos, A., White, S.M., Kundu, M.R., Gary, D.E., 2000b. Observations and models of a flaring loop. ApJ 533, 1053–1062. https://doi.org/10.1086/308705.

Nita, G.M., Fleishman, G.D., Kuznetsov, A.A., et al., 2015. Three-dimensional radio and X-ray modeling and data analysis software: revealing flare complexity. ApJ 799, 236. https://doi.org/10.1088/0004-637X/799/2/236. Available from: <arXiv:1409.0896>.

Nita, G.M., Gary, D.E., Lanzerotti, L.J., Thomson, D.J., 2002. The peak flux distribution of solar radio bursts. ApJ 570, 423–438. https://doi.org/10.1086/339577.

Oberoi, D., Matthews, L.D., Cairns, I.H., et al., 2011. First spectroscopic imaging observations of the Sun at low radio frequencies with the murchison widefield array prototype. ApJ Lett. 728, L27. https://doi.org/10.1088/2041-8205/728/2/L27. Available from: <arXiv:1101.0620>.

Paesold, G., Benz, A.O., Klein, K.-L., Vilmer, N., 2001. Spatial analysis of solar type III events associated with narrow band spikes at metric wavelengths. A&A 371, 333–342. https://doi.org/10.1051/0004-6361:20010358. Available from: <arXiv:astro-ph/0103491>.

Parker, E.N., 1988. Nanoflares and the solar X-ray corona. ApJ 330, 474–479. https://doi.org/10.1086/166485.

Patsourakos, S., Vourlidas, A., 2012. On the nature and genesis of EUV waves: a synthesis of observations from SOHO, STEREO, SDO, and Hinode (Invited Review). Sol. Phys. 281, 187–222. https://doi.org/10.1007/s11207-012-9988-6. Available from: <arXiv:1203.1135>.

Perley, R.A., Chandler, C.J., Butler, B.J., Wrobel, J.M., 2011. The expanded very large array: a new telescope for new science. ApJ Lett. 739, L1. https://doi.org/10.1088/2041-8205/739/1/L1. Available from: <arXiv:1106.0532>.

Pick, M., Démoulin, P., Krucker, S., Malandraki, O., Maia, D., 2005a. Radio and X-ray signatures of magnetic reconnection behind an ejected flux rope. ApJ 625, 1019–1026. https://doi.org/10.1086/429530.

Pick, M., Malherbe, J.-M., Kerdraon, A., Maia, D.J.F., 2005b. On the disk Hα and radio observations of the 2003 October 28 flare and coronal mass ejection event. ApJ Lett. 631, L97–L100. https://doi.org/10.1086/497137.

Pick, M., Mason, G.M., Wang, Y.-M., Tan, C., Wang, L., 2006. Solar source regions for ^{3}He-rich solar energetic particle events identified using imaging radio, optical, and energetic particle observations. ApJ 648, 1247–1255. https://doi.org/10.1086/505926.

Pick, M., Stenborg, G., Démoulin, P., et al., 2016. Homologous solar events on 2011 January 27: build-up and propagation in a complex coronal environment. ApJ 823, 5. https://doi.org/10.3847/0004-637X/823/1/5.

Pick, M., Vilmer, N., 2008. Sixty-five years of solar radioastronomy: flares, coronal mass ejections and Sun Earth connection. A&AR 16, 1–153. https://doi.org/10.1007/s00159-008-0013-x.

Pohjolainen, S., Maia, D., Pick, M., et al., 2001. On-the-disk development of the halo coronal mass ejection on 1998 May 2. ApJ 556, 421–431. https://doi.org/10.1086/321577.

Ramesh, R., Kathiravan, C., Barve, I.V., et al., 2010a. Radio observations of weak energy releases in the solar corona. ApJ Lett. 719, L41–L44. https://doi.org/10.1088/2041-8205/719/1/L41.

Ramesh, R., Kathiravan, C., Sastry, C.V., 2003. Metric radio observations of the evolution of a "Halo" coronal mass ejection close to the Sun. ApJ Lett. 591, L163–L166. https://doi.org/10.1086/377162.

Ramesh, R., Kathiravan, C., Sastry, C.V., 2010b. Estimation of magnetic field in the solar coronal streamers through low frequency radio

observations. ApJ 711, 1029–1032. https://doi.org/10.1088/0004-637X/711/2/1029.
Ramesh, R., Kishore, P., Mulay, S.M., Barve, I.V., Kathiravan, C., Wang, T.J., 2013. Low-frequency observations of drifting, non-thermal continuum radio emission associated with the solar coronal mass ejections. ApJ 778, 30. https://doi.org/10.1088/0004-637X/778/1/30.
Ramesh, R., Lakshmi, M.A., Kathiravan, C., Gopalswamy, N., Umapathy, S., 2012. The location of solar metric Type II radio bursts with respect to the associated coronal mass ejections. ApJ 752, 107. https://doi.org/10.1088/0004-637X/752/2/107.
Ratcliffe, H., Kontar, E.P., Reid, H.A.S., 2014. Large-scale simulations of solar type III radio bursts: flux density, drift rate, duration, and bandwidth. A&A 572, A111. https://doi.org/10.1051/0004-6361/201423731. Available from: <arXiv:1410.2410>.
Reames, D.V., 1999. Particle acceleration at the Sun and in the heliosphere. Space Sci. Rev. 90, 413–491. https://doi.org/10.1023/A:1005105831781.
Reid, H.A.S., Kontar, E.P., 2017. Imaging spectroscopy of type U and J solar radio bursts with LOFAR. A&A 606, A141. https://doi.org/10.1051/0004-6361/201730701. Available from: <arXiv:1706.07410>.
Reid, H.A.S., Ratcliffe, H., 2014. A review of solar type III radio bursts. Res. Astron. Astrophys. 14, 773–804. https://doi.org/10.1088/1674-4527/14/7/003. Available from: <arXiv:1404.6117>.
Reid, H.A.S., Vilmer, N., Kontar, E.P., 2011. Characteristics of the flare acceleration region derived from simultaneous hard X-ray and radio observations. A&A 529, A66. https://doi.org/10.1051/0004-6361/201016181. Available from: <arXiv:1102.2342>.
Reid, H.A.S., Vilmer, N., Kontar, E.P., 2014. The low-high-low trend of type III radio burst starting frequencies and solar flare hard X-rays. A&A 567, A85. https://doi.org/10.1051/0004-6361/201321973. Available from: <arXiv:1403.1839>.
Ryabov, B.I., Maksimov, V.P., Lesovoi, S.V., Shibasaki, K., Nindos, A., Pevtsov, A., 2005. Coronal magnetography of solar active region 8365 with the SSRT and NoRH radio heliographs. Sol. Phys. 226, 223–237. https://doi.org/10.1007/s11207-005-2691-0.
Ryabov, B.I., Pilyeva, N.A., Alissandrakis, C.E., Shibasaki, K., Bogod, V. M., Garaimov, V.I., Gelfreikh, G.B., 1999. Coronal magnetography of an active region from microwave polarization inversion. Sol. Phys. 185, 157–175. https://doi.org/10.1023/A:1005114303703.
Saint-Hilaire, P., Vilmer, N., Kerdraon, A., 2013. A decade of solar Type III radio bursts observed by the Nançay Radioheliograph 1998-2008. ApJ 762, 60. https://doi.org/10.1088/0004-637X/762/1/60. Available from: <arXiv:1211.3474>.
Sastry, C.V., 2009. Polarization of the thermal radio emission from outer solar corona. ApJ 697, 1934–1939. https://doi.org/10.1088/0004-637X/697/2/1934.
Schmidt, J.M., Cairns, I.H., 2014. Type II solar radio bursts predicted by 3-D MHD CME and kinetic radio emission simulations. J. Geophys. Res. (Space Phys.) 119, 69–87. https://doi.org/10.1002/2013JA019349.
Schmidt, J.M., Cairns, I.H., 2016. Quantitative prediction of type II solar radio emission from the Sun to 1 AU. GRL 43, 50–57. https://doi.org/10.1002/2015GL067271.
Sharma, R., Oberoi, D., Arjunwadkar, M., 2018. Quantifying weak nonthermal solar radio emission at low radio frequencies. ApJ 852, 69. https://doi.org/10.3847/1538-4357/aa9d96. Available from: <arXiv:1709.00878>.
Sheridan, K.V., 1978. Some recent explorations of the solar corona from the Culgoora Solar Radio Observatory. Proc. Astron. Soc. Australia 3, 185–194. https://doi.org/10.1017/S132335800002453X.
Shibasaki, K., Alissandrakis, C.E., Pohjolainen, S., 2011. Radio emission of the quiet Sun and active regions (invited review). Sol. Phys. 273, 309–337. https://doi.org/10.1007/s11207-011-9788-4.
Shibasaki, K., Enome, S., Nakajima, H., et al., 1994. A purely polarized S-component at 17 GHz. PASJ 46, L17–L20.
Simões, P.J.A., Costa, J.E.R., 2010. Gyrosynchrotron emission from anisotropic pitch-angle distribution of electrons in 3-D solar flare sources. Sol. Phys. 266, 109–121. https://doi.org/10.1007/s11207-010-9596-2.
Slottje, C., 1978. Millisecond microwave spikes in a solar flare. Nature 275, 520–521. https://doi.org/10.1038/275520a0.
Spangler, S.R., Whiting, C.A., 2009. Radio remote sensing of the corona and the solar wind. In: Universal Heliophysical Processes. In: Gopalswamy, N., Webb, D.F. (Eds.), . IAU Symposium, vol. 257. Cambridge University Press, Cambridge, pp. 529–541. https://doi.org/10.1017/S1743921309029834. Available from: <arXiv:0809.4645>.
Stewart, R.T., Dulk, G.A., Sheridan, K.V., House, L.L., Wagner, W.J., Illing, R., Sawyer, C., 1982. Visible light observations of a dense plasmoid associated with a moving Type IV solar radio burst. A&A 116, 217–223.
Suresh, A., Sharma, R., Oberoi, D., et al., 2017. Wavelet-based characterization of small-scale solar emission features at low radio frequencies. ApJ 843, 19. https://doi.org/10.3847/1538-4357/aa774a. Available from: <arXiv:1612.01016>.
Suzuki, S., Dulk, G.A., 1985. Bursts of Type III and Type V. In: McLean, D.J., Labrum, N.R. (Eds.), Solar Radiophysics: Studies of Emission from the Sun at Metre Wavelengths, pp. 289–332.
Swarup, G., Ananthakrishnan, S., Kapahi, V.K., Rao, A.P., Subrahmanya, C.R., Kulkarni, V.K., 1991. The giant metre-wave radio telescope. Curr. Sci. 60 (2/JAN25), 95–105.
Tapping, K.F., Kuijpers, J., Kaastra, J.S., et al., 1983. VLBI of solar flares. A&A 122, 177–180.
Tingay, S.J., Oberoi, D., Cairns, I., et al., 2013. The Murchison Widefield Array: solar science with the low frequency SKA Precursor. Journal of Physics Conference Series, vol. 440, p. 012033. https://doi.org/10.1088/1742-6596/440/1/012033. Available from: <arXiv:1301.6414>.
Tritschler, A., Rimmele, T.R., Berukoff, S., et al., 2015. DKIST: observing the Sun at high resolution. In: 18th Cambridge Workshop on Cool Stars, Stellar Systems, and the Sun. In: van Belle, G.T., Harris, H.C. (Eds.), . Cambridge Workshop on Cool Stars, Stellar Systems, and the Sun, vol. 18, pp. 933–944.
Tsiklauri, D., 2011. An alternative to the plasma emission model: particle-in-cell, self-consistent electromagnetic wave emission simulations of solar type III radio bursts. Phys. Plasmas 18, 052903. https://doi.org/10.1063/1.3590928. Available from: <arXiv:1011.5832>.
Tun, S.D., Gary, D.E., Georgoulis, M.K., 2011. Three-dimensional structure of a solar active region from spatially and spectrally resolved microwave observations. ApJ 728, 1. https://doi.org/10.1088/0004-637X/728/1/1.
Tun, S.D., Vourlidas, A., 2013. Derivation of the magnetic field in a coronal mass ejection core via multi-frequency radio imaging. ApJ 766, 130. https://doi.org/10.1088/0004-637X/766/2/130.
Tun Beltran, S.D., Cutchin, S., White, S., 2015. A new look at Type-III bursts and their use as coronal diagnostics. Sol. Phys. 290, 2423–2437. https://doi.org/10.1007/s11207-015-0760-6. Available from: <arXiv:1508.00206>.
Tzatzakis, V., Nindos, A., Alissandrakis, C.E., 2008. A statistical study of microwave flare morphologies. Sol. Phys. 253, 79–94. https://doi.org/10.1007/s11207-008-9263-z.
Vainio, R., Desorgher, L., Heynderickx, D., et al., 2009. Dynamics of the Earth's particle radiation environment. Space Sci. Rev. 147, 187–231. https://doi.org/10.1007/s11214-009-9496-7.
Valtonen, E., 2011. Solar energetic particles. In: Miralles, M.P., Sánchez Almeida, J. (Eds.), The Sun, the Solar Wind, and the Heliosphere. Springer, Dordrecht, pp. 167–176.
van Ballegooijen, A.A., Asgari-Targhi, M., Cranmer, S.R., DeLuca, E.E., 2011. Heating of the solar chromosphere and corona by Alfvén wave turbulence. ApJ 736, 3. https://doi.org/10.1088/0004-637X/736/1/3. Available from: <arXiv:1105.0402>.
van Haarlem, M.P., Wise, M.W., Gunst, A.W., et al., 2013. LOFAR: the LOw-Frequency ARray. A&A 556, A2. https://doi.org/10.1051/0004-6361/201220873. Available from: <arXiv:1305.3550>.
Vršnak, B., Cliver, E.W., 2008. Origin of coronal shock waves. Invited review. Sol. Phys. 253, 215–235. https://doi.org/10.1007/s11207-008-9241-5.
Wang, H., Gary, D.E., Lim, J., Schwartz, R.A., 1994. Miocrowave spectral imaging, H-alpha and hard X-ray observations of a solar limb flare. ApJ 433, 379–388. https://doi.org/10.1086/174652.

Warmuth, A., Mann, G., Aurass, H., 2009. Modelling shock drift acceleration of electrons at the reconnection outflow termination shock in solar flares. Observational constraints and parametric study. A&A 494, 677–691. https://doi.org/10.1051/0004-6361:200810101.

White, S.M., 1999. Radio versus EUV/X-ray observations of the solar atmosphere. Sol. Phys. 190, 309–330. https://doi.org/10.1023/A:1005253501584.

White, S.M., Benz, A.O., Christe, S., et al., 2011. The relationship between solar radio and hard X-ray emission. Space Sci. Rev. 159, 225–261. https://doi.org/10.1007/s11214-010-9708-1. Available from: <arXiv:1109.6629>.

White, S.M., Kundu, M.R., 1997. Radio observations of gyroresonance emission from coronal magnetic fields. Sol. Phys. 174, 31–52. https://doi.org/10.1023/A:1004975528106.

White, S.M., Kundu, M.R., Garaimov, V.I., Yokoyama, T., Sato, J., 2002. The physical properties of a flaring loop. ApJ 576, 505–518. https://doi.org/10.1086/341621.

White, S.M., Kundu, M.R., Shimizu, T., et al., 1995. The radio properties of solar active region soft X-ray transient brightenings. ApJ 450, 435–440. https://doi.org/10.1086/176153.

Xu, Y., Emslie, A.G., Hurford, G.J., 2008. RHESSI hard X-ray imaging spectroscopy of extended sources and the physical properties of electron acceleration regions in solar flares. ApJ 673, 576–585. https://doi.org/10.1086/524184.

Yan, Y., Chen, L., Yu, S., 2016. First radio burst imaging observation from Mingantu Ultrawide Spectral Radioheliograph. In: Solar and Stellar Flares and their Effects on Planets. In: Kosovichev, A.G., Hawley, S.L., Heinzel, P. (Eds.), . IAU Symposium, vol. 320. Cambridge University Press, Cambridge, pp. 427–435. https://doi.org/10.1017/S174392131600051X.

Zharkova, V.V., Arzner, K., Benz, A.O., et al., 2011. Recent advances in understanding particle acceleration processes in solar flares. Space Sci. Rev. 159, 357–420. https://doi.org/10.1007/s11214-011-9803-y. Available from: <arXiv:1110.2359>.

Zheleznyakov, V.V., 1962. The origin of the slowly varying component of solar radio emission. Soviet Astr. 6, 3–9.

Zheleznyakov, V.V., 1970. Radio Emission of the Sun and Planets. Pergamon Press, Oxford.

Zimovets, I.V., Sadykov, V.M., 2015. Spatially resolved observations of a coronal type II radio burst with multiple lanes. Adv. Space Res. 56, 2811–2832. https://doi.org/10.1016/j.asr.2015.01.041.

Zucca, P., Carley, E.P., Bloomfield, D.S., Gallagher, P.T., 2014a. The formation heights of coronal shocks from 2D density and Alfvén speed maps. A&A 564, A47. https://doi.org/10.1051/0004-6361/201322650. Available from: <arXiv:1402.4051>.

Zucca, P., Pick, M., Démoulin, P., et al., 2014b. Understanding coronal mass ejections and associated shocks in the solar corona by merging multiwavelength observations. ApJ 795, 68. https://doi.org/10.1088/0004-637X/795/1/68. Available from: <arXiv:1409.3691>.